Chapter 4
Atomic Movies of Laser-Induced Structural and Phase Transformations from Molecular Dynamics Simulations

Chengping Wu, Eaman T. Karim, Alexey N. Volkov and Leonid V. Zhigilei

Abstract Molecular dynamics (MD) simulations of laser-materials interactions are playing an important role in investigation of complex and highly non-equilibrium processes involved in short pulse laser processing and surface modification. This role is defined by the ability of MD simulations to reveal in-depth information on the structural and phase transformations induced by the laser excitation and, at the same time, to provide clear visual representations, or "atomic movies," of laser-induced dynamic processes. This chapter provides a brief overview of recent progress in the description of laser coupling and relaxation of photo-excited states in metals, semiconductors, insulators and molecular systems within the general framework of the classical MD technique and presents several examples of MD simulations of laser melting, generation of crystal defects, photomechanical spallation, explosive boiling and molecular entrainment in laser ablation. Possible directions of future progress in atomistic modeling of laser-materials interactions and the potential role of MD simulations in the design of an integrated multiscale computational model capable of accounting for interrelations between processes occurring at different time- and length-scales are discussed.

4.1 Introduction

Computer modeling is playing an increasingly important role in the development of the theoretical understanding of laser-materials interactions and the advancement of laser applications. The need for computer modeling is amplified by the complexity of the material response to the rapid laser energy deposition. Short pulse laser irradiation brings the target material to a state of strong electronic, thermal, and

C. Wu · E. T. Karim · A. N. Volkov · L. V. Zhigilei (✉)
Department of Materials Science and Engineering, University of Virginia,
395 McCormick Road, Charlottesville, VA 22904-4745, USA
e-mail: lz2n@virginia.edu

M. Castillejo et al. (eds.), *Lasers in Materials Science*,
Springer Series in Materials Science 191, DOI: 10.1007/978-3-319-02898-9_4,

mechanical non-equilibrium and triggers a cascade of interrelated processes that may involve structural and phase transformations, such as melting and resolidification, generation of crystal defects, fracture and disintegration of the region of the laser energy deposition due to photomechanical stresses (front surface spallation), vaporization and explosive boiling of strongly overheated surface region, ionization and plasma formation. Computer modeling of this diverse range of processes is challenging and requires a combination of different computational techniques.

Computational models used in the simulations of laser-materials interactions can be separated into three distinct groups: (1) quantum mechanics based (ab initio) electronic structure calculation methods, (2) classical atomistic and coarse-grained MD techniques, and (3) continuum-level kinetic and hydrodynamic models.

The electronic structure calculations are capable of reproducing the initial material response to the laser excitation, including transient changes in interatomic bonding and corresponding modifications of material properties [1–3], non-thermal structural transformations [3–8], bond-breaking/rearrangement and atomic ejection under conditions of strong electronic excitation [9–11], as well as relaxation of excited states and electron–phonon equilibration [12, 13]. The high computational cost of electronic structure calculations, however, limits the size of the computational systems treated in ab initio simulations to several hundreds of atoms, thus preventing realistic modeling of laser-induced structural and phase transformations.

Continuum models of laser-materials interactions, on the other hand, are capable of computationally efficient treatment of laser-induced processes at experimental time and length-scales. These models are typically based on the solution of a set of partial differential equations describing the laser energy deposition, heat transfer, thermoelastic and plastic deformation, photolytic and pyrolytic chemical reactions, phase transformations (melting, resolidification, vaporization and volume ablation processes), as well as ablation plume expansion, e.g., [14–24]. Hydrodynamic models that adopt multi-phase equations of state to describe the evolution of thermodynamic parameters of the material have also been used for simulation of laser-induced phase transformations, including photomechanical spallation, vaporization, and ablation [25–33]. The predictive power of the continuum-level models, however, is limited by the need for a priory knowledge of all the processes that may take place during the simulations. The fundamental understanding of the mechanisms and kinetics of complex and highly non-equilibrium structural and phase transformations occurring in the irradiated target is often lacking, making it difficult to design a reliable continuum description of laser-materials interactions.

Given the limitations of the continuum and ab initio approaches to modeling of laser-materials interactions, classical MD simulation technique [34–36] has emerged as a promising alternative approach capable of providing insights into collective atomic dynamics responsible for laser-induced structural and phase transformations. The MD technique is based on the numerical integration of the classical equations of motion for all atoms in the system. The interatomic interaction is described by a potential energy function that defines the equilibrium structure and thermodynamic properties of the material. The interatomic potentials

are often designed with the help of ab initio simulations and are fitted to reproduce some of the basic properties of the materials of interest (e.g., elastic moduli, cohesive energy, energies of formation/migration of point defects, coefficient of thermal expansion, melting temperature). Once the interatomic potential is chosen and the initial conditions (positions and velocities of all particles in the system) are defined, the equations of motion for all atoms are solved numerically and atomic trajectories (positions and velocities as a function of time) are obtained. The main strength of the MD method is that it does not require any assumptions about the processes taking place in the systems that are investigated. This characteristic of the MD technique presents a significant advantage over the continuum-level methods where all relevant processes have to be known (and described mathematically) before the simulations can be performed.

The atomic trajectories generated in MD simulations provide a clear visual picture, or "atomic movies," of the laser-induced processes and, at the same time, can be used to study the evolution of temperature, pressure, structure and phase state of the irradiated material, thus revealing complete mechanistic information on the complex phenomenon of laser-materials interactions. The MD technique has been actively used in investigations of laser melting and resolidification [37–48], generation of crystal defects [49–51], photomechanical spallation [40, 45, 48, 52–58], and ablation [39, 43, 45, 48, 52, 59–91] of various material systems.

A comprehensive review of the applications of the MD technique to simulation of laser-materials interactions has been provided in a book published as a follow up on the first Venice School on Lasers in Materials Science [36]. In this chapter, therefore, the discussion of the computational models in Sect. 4.2 is limited to a brief overview of methods developed for the description of laser coupling to different materials and relaxation of photo-excited states within the classical atomistic or coarse-grained MD technique. Recent results from simulations of laser melting, generation of crystal defects (dislocations, vacancies and interstitials), photomechanical spallation, explosive boiling and molecular entrainment in laser ablation are discussed in Sect. 4.3. The ability of MD simulations to provide visual representations of laser-induced dynamic processes is highlighted by providing series of snapshots taken at different moments during the MD simulations. Finally, in Sect. 4.4, the potential role of the classical MD simulations in the general approach of multiscale modeling of laser-materials interactions is discussed.

4.2 Representation of Laser Excitation in Classical Molecular Dynamics

The interatomic interactions, described in classical MD by pair or many-body potential energy functions [92–94], are ultimately defined by the electronic structures of the materials. The electrons and quantum effects, however, are not explicitly represented in the classical MD method. Therefore, the optical properties

of an irradiated material, as well as the mechanisms and kinetics of the relaxation of optically excited states, can not be obtained in the course of an MD simulation, but have to be assumed prior to the simulation and incorporated into the model. The diversity of physical mechanisms of laser coupling and relaxation/thermalization of the absorbed laser energy necessitates the design of material-specific computational approaches for the description of the laser excitation within the general framework of the classical MD method. A brief overview of computational models developed for MD simulations of laser interactions with molecular systems, metals, semiconductors and insulators is provided below.

In molecular systems, photoexcitation of a particular vibrational mode or a group of modes can occur through direct resonant absorption of infrared (IR) irradiation [95] or internal conversion of molecular chromophores electronically excited by ultraviolet (UV) irradiation. The vibrational excitation is followed by a rapid, within picoseconds, intra-molecular redistribution of the deposited energy within the excited molecule [96, 97] and a slower, within tens to hundreds of picoseconds, inter-molecular energy transfer leading to the vibrational cooling of the excited molecule [98–100].

The relatively fast, compared to the timescale of the collective molecular ejection in laser ablation, rate of the vibrational thermalization of the deposited laser energy may serve as a justification for simulation of the laser excitation by fast temperature increase in the surface region of the irradiated target, an approach adopted in a number of atomistic MD simulations of short pulse laser ablation of molecular targets [65, 71, 101]. An internal vibrational excitation followed by the dynamic energy transfer to the translational degrees of freedom has been used in simulations of laser-induced molecular desorption from an oxygen crystal [102].

The finite rate of the vibrational relaxation of photo-excited molecules is accounted for in a coarse-grained "breathing sphere" model developed for simulation of laser interactions with molecular targets [60, 75]. In this model, each molecule is represented by a spherical particle, with parameters of inter-particle interaction potential chosen to approximately reproduce the physical properties of a molecular target. In order to simulate molecular excitation by photon absorption and vibrational relaxation of the excited molecules, an additional internal degree of freedom is added to each molecule by allowing the particles to change their radii, or to "breathe." The laser irradiation is simulated by vibrational excitation of molecules that are randomly chosen during the laser pulse duration within the penetration depth appropriate for a given wavelength. The vibrational excitation is modeled by depositing a quantum of energy equal to the photon energy into the kinetic energy of the internal breathing mode of a given molecule. In the case of UV laser irradiation, the breathing mode can be considered as the recipient of the energy released by internal conversion from electronically excited states. The parameters of a potential function attributed to the internal motion control the characteristic frequency of the breathing mode and, as a result, define the rate of the conversion of the internal energy of the molecules excited by the laser to the translational and internal motions of the surrounding molecules. The breathing sphere model has been actively used in investigations of laser desorption, ablation,

and spallation of molecular targets [52, 53, 55, 60–62, 66–69, 74, 75] and polymer solutions [72, 86, 87, 103, 104]. A description of ionization mechanisms has also been included into the breathing sphere model and used for investigation of the processes that control the yield of ions in matrix-assisted laser desorption/ionization (MALDI) mass spectrometry technique [105–107]. Several examples of the applications of the coarse-grained MD to investigation of laser ablation of molecular targets, including polymer and carbon nanotube solutions, are provided in Sects. 4.3.4 and 4.3.5.

An alternative result of the photon absorption, photodissociation of the excited molecule into fragments, has also been considered in coarse-grained MD simulations. In early simulations of laser ablation of polymer targets, the pressure generated by products of photolytic reactions is reproduced through activation of repulsive interactions between the molecules in the absorption region of the target [108, 109]. More recently, a methodology for semi-quantitative representation of photochemical reactions (bond scission followed by abstraction and recombination reactions) within the coarse-grained MD model has been developed and applied for investigation of UV laser ablation of a chlorobenzene [70, 75, 110] and poly(methyl methacrylate) [81, 88].

Substrate-assisted laser-driven ejection of a layer of volatile molecular or atomic material has been investigated in MD simulations performed for various systems, including a water ice film deposited on a Au substrate [111–113], a generic fluid-substrate two-dimensional system [114], a liquid Ar film deposited on a Pt substrate [115, 116], and a solid Xe overlayer deposited on a Si substrate [117]. The laser energy deposition is simulated by instantaneous [111, 112, 114–116] or gradual [113] temperature increase in the substrate. A realistic temperature profile defined by the laser heating and cooling due to the thermal conduction to the bulk of the substrate has also been simulated by solving the heat conduction equation with a source term describing irradiation of a Si substrate by a 5 ns laser pulse [117]. The simulations suggest that energy transfer from an absorbing substrate to a transparent layer can result in superheating and fast vaporization (or explosive boiling) of a part of the layer adjacent to the hot substrate, leading to the separation and ejection of the layer from the substrate.

In metals, the absorption of laser light by the conduction band electrons is followed by quick, within femtoseconds, equilibration among the electrons (establishment of Fermi-Dirac distribution) and slower, from fractions of a picosecond to several tens of picoseconds (depending on the strength of electron–phonon coupling [118]), equilibration between the electrons and atomic vibrations (phonons). Several computational approaches have been developed for the description of the electronic excitation, thermalization of the absorbed laser energy, and electron contribution to the heat conduction in metals within the framework of the classical MD method [38, 40, 58, 73, 79, 119–121]. In particular, the model suggested in [40, 73], is based on the well-known two-temperature model (TTM) [122] that describes the time evolution of the lattice and electron temperatures in the irradiated target by two coupled nonlinear differential equations. In the combined TTM–MD model, MD substitutes the TTM equation for the

lattice temperature. The TTM equation for the electron temperature is solved by a finite difference method simultaneously with MD integration of the equations of motion of atoms. The electron temperature enters a coupling term that is added to the MD equations of motion to account for the energy exchange between the electrons and the lattice. The cells in the finite difference discretization are related to the corresponding volumes of the MD system, and the local lattice temperature is defined for each cell from the average kinetic energy of thermal motion of atoms. In simulations of laser intertactions with bulk targets, e.g., [45, 46, 48, 49, 51, 55], the atomistic representation is used only in the surface region of the target, where active processes of laser melting, resolidification and/or ablation take place, whereas the heat transfer in the deeper region of the target is represented by the conventional TTM or one-temperature thermal diffusion equation. The TTM–MD model has been successfully applied for investigation of laser melting [38, 40–42, 44–48], generation of crystal defects [49–51], photomechanical spallation and ablation [40, 45, 48, 55, 58, 73, 78, 79, 90, 91] of metal targets. Several examples of the applications of the TTM–MD model are provided in Sects. 4.3.1–4.3.3.

The adaptation of classical MD for simulation of laser interactions with semiconductors and insulators is more challenging compared to metals, as the models should account for the formation and diffusion of electron-hole pairs, localized weakening of interatomic bonding, ionization and generation of free electrons, absorption of the laser energy by the free electrons, as well as the energy coupling between the excited electrons and ions. First models developed for Si are based on a local treatment of individual excitation events and include a description of bond weakening, ionization and electron–ion recombination [64, 123], as well as transition of Si to the metallic state upon melting and a stochastic (Monte Carlo) treatment of carrier diffusion and scattering [76, 82]. The development of atomistic models for laser interaction with insulators has been limited to exploratory work for fused silica [124] and LiF [125] films, where a continuum description of the laser coupling and generation of free electrons is combined with MD treatment of atoms that accounts for the energy transfer from the excited electrons to ions [124, 125] and local changes in interatomic interactions due to the ionization [124].

4.3 Atomic Movies from MD Simulations of Laser-Material Interactions

One of the main advantages of the MD technique is in its ability to provide complete atomic-level information on the material response to short pulse laser irradiation. A mere visual analysis of snapshots obtained in MD simulations is often sufficient for drawing preliminary ideas on the physical processes responsible for laser material modification or removal. These ideas can then be used to design more advanced data analysis methods capable of quantitative thermodynamic or structural characterization of the laser-induced processes. In this section, we

exploit the ability of the MD method to provide the atomic-level "movies" of the material behavior under conditions of fast laser energy deposition to develop a better intuitive understanding of the mechanisms of laser melting, generation of crystal defects, photomechanical spallation and ablation of irradiated targets.

4.3.1 Laser Melting

Although melting is a common and well-studied phenomenon that plays a prominent role in many laser processing applications, the microscopic mechanisms and kinetics of laser-induced melting has been and still remain subjects of active discussions in literature, e.g., [41, 126–136]. Under conditions of slow energy deposition by long (nanoseconds and longer) laser pulses, the melting process starts from surfaces and internal crystal defects and proceeds by propagation of melting fronts at low levels of superheating above the equilibrium melting temperature, T_m. The kinetic description of the melting process in this case reduces to a linear relationship between the velocity of the melting front and the superheating [137, 138], or the melting process is considered to be heat flow limited and the superheating at the melting front is neglected altogether. Irradiation by short (pico- and femtosecond) laser pulses, however, can result in extremely high heating rates exceeding 10^{14} K/s, making the time of the temperature increase shorter than the time needed for any significant advancement of the melting front. The homogeneous nucleation of liquid regions inside the superheated crystal can be expected to make the dominant contribution to the melting process induced by the short laser pulses.

Experimental probing of the short pulse laser melting with optical, X-ray and electron diffraction time-resolved techniques have provided valuable information on the characteristic time-scales and mechanisms of melting occurring under conditions of strong superheating [126–135]. The important role of MD simulations has been to provide detailed atomic-level information on the rapid laser-induced phase transformations in the irradiated targets and to assist in interpretation of the results of the experimental probing. Indeed, MD simulations of laser melting and resolidification of bulk metal targets and thin films of various thickness [37–51] has revealed a wealth of information on the microscopic mechanisms and kinetics of laser melting. In particular, the relative contributions of the homogeneous and heterogeneous melting mechanisms have been analyzed and related to the irradiation conditions in simulations performed for different metals (Ni, Au, Al, Cu and Cr), target geometries (thin films [40–42, 44, 47, 50, 56], bulk targets [45, 48, 49] and metal bilayer systems [46, 51]), and laser pulse durations (from 200 fs to 150 ps). The lattice distortions associated with relaxation of laser-induced stresses have been found to significantly reduce the crystal stability against melting, resulting in homogeneous nucleation of the liquid phase at temperatures close to the equilibrium melting temperature [41]. The calculations of the changes in the diffraction profiles and density correlation functions during the melting process [44]

have been used to establish direct connections between the results of MD simulations and time-resolved electron diffraction experiments [129, 131, 132].

The atomic-level view of the two distinct melting mechanisms identified in MD simulations, heterogeneous melting by propagation of melting fronts from external surfaces of the target and homogeneous melting by nucleation of liquid regions inside a strongly superheated crystalline material, is provided in Fig. 4.1a, b, where snapshots from two simulations performed for a 20 nm single crystal Au film irradiated with a 200 fs laser pulse are shown for absorbed fluences of 45 and 180 J/m^2 [47]. In both simulations, the ballistic energy transfer by nonthermal electrons and relatively weak electron–phonon coupling in Au result in the establishment of a uniform distribution of the electron and lattice temperatures throughout the 20 nm film during the time of the electron–phonon equilibration. At a fluence of 45 J/m^2 (Fig. 4.1a), the lattice temperature increases due to the electron–phonon energy exchange and reaches the maximum value of 1.16 T_m by the time of $\sim$20 ps. Two melting fronts emerge from the free surfaces of the film and propagate toward the center of the film. The velocities of the melting fronts gradually decrease from their maximum values of $\sim$100 m/s down to zero as the temperature decreases (due to transformation of the thermal energy to the heat of melting) and eventually saturates at T_m by the time of 500 ps. The snapshot shown in Fig. 4.1a for 500 ps corresponds to the final state of the partially melted film with a crystalline layer located in the middle. At a higher fluence of 180 J/m^2 (Fig. 4.1b), the high level of the electronic excitation leads to a transient increase of the strength of the electron–phonon coupling [118] and to a much faster lattice heating. By the time of 2 ps the lattice temperature exceeds the level of $\sim$1.25 T_m that corresponds to the limit of thermal stability of the crystal lattice [41, 44, 136, 139, 140], resulting in a rapid collapse of the crystal structure within the next several picoseconds. Rapid nucleation and growth of liquid regions throughout the film are preceded by thermally activated generation of a large number of vacancy-interstitial pairs that can be identified in the snapshots shown for the time of 4 ps in Fig. 4.1b. The high density of point defects introduces lattice distortions and reduces stability of the crystal structure against melting [47].

The effect of high density of grain boundaries in nanocrystalline metals on the characteristics of the laser melting process is illustrated in Fig. 4.1c, d, where snapshots from MD simulations performed for Au films with nanocrystalline structure are shown for the same irradiation conditions as the ones discussed above for single crystal films. Although at all laser fluences the melting process starts from the grain boundary regions as soon as the lattice temperature approaches and exceeds the equilibrium melting temperature, the contribution of the grain boundary melting to the overall melting process is very different in the low fluence regime (below or close to the threshold for the complete melting of the film) and in the high fluence regime (significantly above the melting threshold).

At low laser fluences, when the maximum lattice temperature does not exceed the limit of crystal stability against homogeneous melting, the microstructure of the film is found to have a much stronger effect on the characteristics of the melting process. In particular, in contrast with the partial melting of about a half of

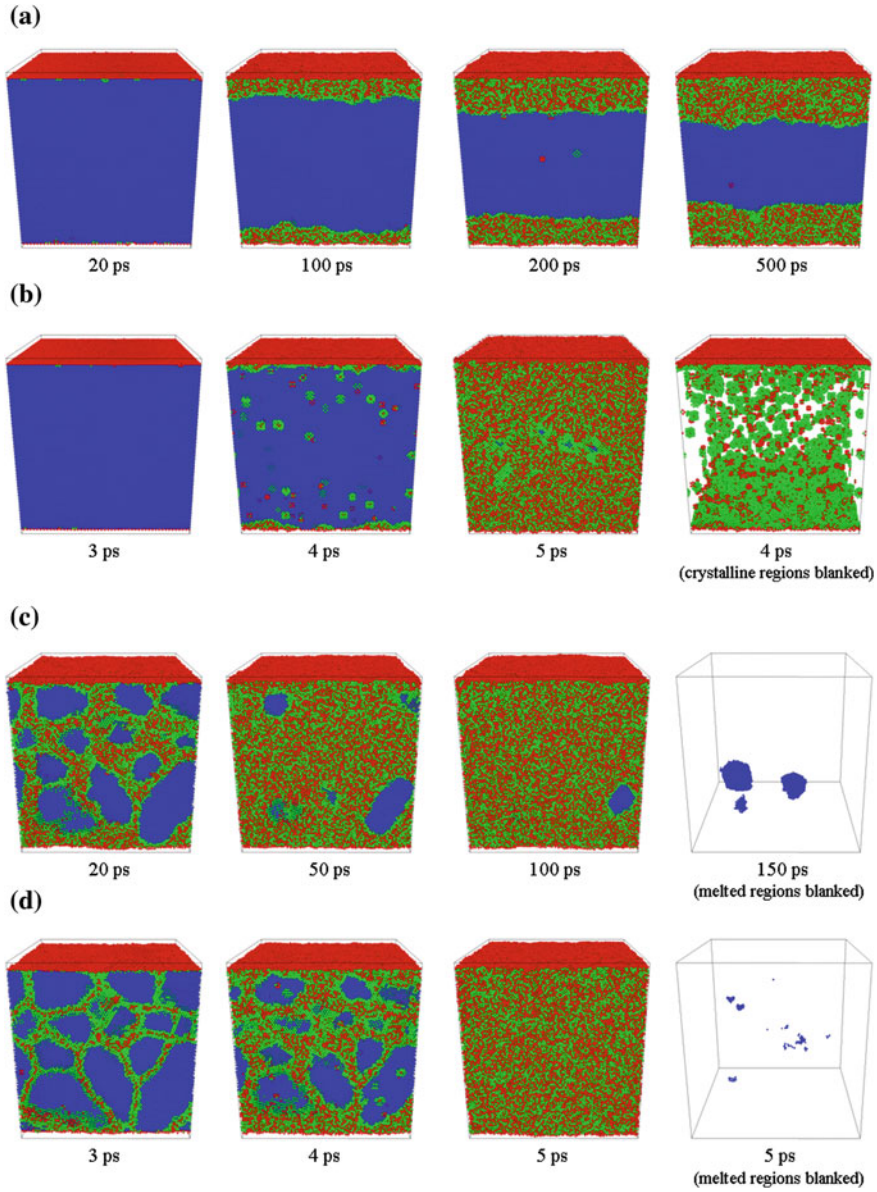

Fig. 4.1 Snapshots of atomic configurations generated in TTM–MD simulations of the melting process in a 20 nm single crystal (**a**, **b**) and nanocrystalline (**c**, **d**) Au films irradiated by 200 fs laser pulses at absorbed fluences of 45 J/m^2 (**a**, **c**) and 180 J/m^2 (**b**, **d**). Atoms are colored according to the local structure: *blue* atoms have local crystalline surroundings, *red* and *green* atoms are at the free surfaces, near crystal defects (grain boundaries, vacancies and interstitials) or belong to the liquid phase. In the *right panel* of (**b**), the atoms in the crystalline parts of the film are blanked to provide a clear view of the emerging point defects and disordered regions. In the *right panels* of (**c**) and (**d**), the atoms that belong to the liquid phase are blanked to expose the remaining crystalline regions. The interstitials and vacancies show up in the snapshots as *large green clusters* and *smaller red clusters*, respectively. The simulations of laser melting of Au films are discussed in [47]

a 20 nm single crystal Au film illustrated in Fig. 4.1a, the nanocrystalline film undergoes complete melting at the same absorbed fluence of 45 J/m^2, Fig. 4.1c. Surprisingly, the melting of the nanocrystalline film is found to continue even after the temperature of the film drops below the equilibrium melting temperature at $\sim$30 ps and the last crystalline regions (e.g., the ones shown in the right panel in Fig. 4.1c) continue to shrink under conditions of about 6 % undercooling below the melting temperature and disappear by a time of 250 ps. This unusual melting behavior of the nanocrystalline films is explained in [47] based on thermodynamic analysis of the stability of small crystalline clusters surrounded by undercooled liquid.

At high laser fluences, e.g., Fig. 4.1d, the kinetics and mechanisms of melting are only weakly affected by the nanocrystalline structure of the film. Although the grain boundary melting in nanocrystalline films results in a moderate decrease of the size of the crystalline grains at the initial stage of the laser heating, the overall timescale of the melting process is largely defined by the fast temperature increase and rapid (within several picoseconds) collapse of the crystal structure as soon as the lattice temperature exceeds the limit of superheating [41, 44, 47, 136, 139, 140].

4.3.2 Generation of Crystal Defects

The fast rate of energy deposition in short pulse laser processing applications may result not only in the rapid melting and resolidification of a surface region of an irradiated target but also lead to the generation of strong compressive stresses. The laser-induced stresses are particularly high in the regime of stress confinement [45, 52, 55, 75, 141–145], when the time of the laser heating (defined by the laser pulse duration, τ_p, or the time of the electron–phonon equilibration, τ_{e-ph}, whichever is longer) is shorter than the time required for the mechanical relaxation (expansion) of the heated volume, $\tau_s \sim L_p/C_s$, where C_s is the speed of sound in the target material and L_p is the effective depth of the laser energy deposition (optical penetration depth or, in the case of metals, the depth of diffusive/ballistic energy transport during the time of the electron–phonon equilibration [42, 45, 55]). The relaxation of the laser induced stresses, taking place simultaneously with melting and resolidification of the surface region of the irradiated target, can result in the generation of a high density of crystal defects (vacancies, interstitials, dislocations, grain boundaries) and corresponding modification of physical and mechanical properties of the surface layer.

Small size of the laser-modified region (on the order 100s of nm) in femtosecond and picosecond laser processing of metals enables, with appropriate design of boundary conditions, the direct MD modeling of the laser-induced generation of crystal defects. Indeed, the emission of partial dislocations from the melting front [36, 146], plastic deformation of films heated by a laser pulse [147], generation of nanocrystalline structure [50] and dislocations [43, 63] around regions of localized laser energy deposition, strong supersaturation of a surface layer with vacancies

[49], and transformation of a lattice-mismatched interface into a three-dimensional periodic array of stacking fault pyramids outlined by stair-rod partial dislocations [51] have been observed in MD simulations. In two examples considered below, the generation of a region of high vacancy concentration and the emission of partial dislocations from a melting front are illustrated by the results of TTM–MD simulations performed for bulk Cr and Ag targets.

The generation of vacancies in a surface region of a Cr target experiencing transient melting and rapid resolidification in response to the irradiation by a 200 fs laser pulse at an absorbed fluence of 850 J/m^2 is illustrated in snapshots shown in Fig. 4.2. The atoms that retain the original body-centered cubic (bcc) local structure are blanked in the snapshots to provide a clear view of the crystal defects and the melted part of the target. The first snapshot is taken at 40 ps after the laser pulse, the time when the depth of the melted layer reaches its maximum. The red spot in the lower part of the melted layer corresponds to a void generated during the passage of the tensile component of the laser-induced stress wave through the liquid–crystal interface. The void collapses by about 90 ps after the laser pulse and is not present in the snapshot shown for 120 ps. As discussed in Sect. 4.3.3, at higher laser fluences the growth and coalescence of voids can result in the separation (spallation) and ejection of a liquid layer from the target. The fluence of 850 J/m^2, however, is just below the threshold for laser spallation of the Cr target [48]. A strong temperature gradient created in the surface region of the target by the short pulse laser irradiation results in a fast cooling and epitaxial resolidification of the melted region. The solidification front advances with velocity that increases with increasing degree of undercooling below the equilibrium melting temperature and reaches its maximum value of about 80 m/s by the end of the resolidification process at about 330 ps, when the temperature at the solidification fronts drops down to about 0.8 T_m.

Two types of crystal defects can be identified in the snapshots shown in Fig. 4.2. The first type is exhibited by atomic planes with elevated energy appearing below the melted region in the snapshot shown for 40 ps. Detailed analysis of the atomic configurations [49] reveals that these planes correspond to the intrinsic stacking faults generated as a result of multiple internal slips on {110} crystallographic planes in response to the rapid uniaxial expansion of the crystal during the dynamic relaxation of the laser-induced stresses. The intrinsic stacking faults are unstable in an unstrained bcc crystal [49, 148] and disappear shortly after the tensile component of the laser-induced stress wave leaves the surface region of the target. Only isolated islands of the stacking faults can be observed in the snapshot shown for 120 ps and no stacking faults are present after 160 ps. The second type of crystal defects is vacancies that appear as clusters of atoms with elevated energy in the snapshots shown in Fig. 4.2. The vacancies are largely concentrated in the region of the target that experienced transient melting and resolidification (above the dashed line in the snapshots). The distribution of vacancies in the top 40 nm surface region of the target at the end of the simulation is shown in Fig. 4.3. The distribution confirms that the overwhelming majority of vacancies are located in the resolidified part of the target. Analysis of the

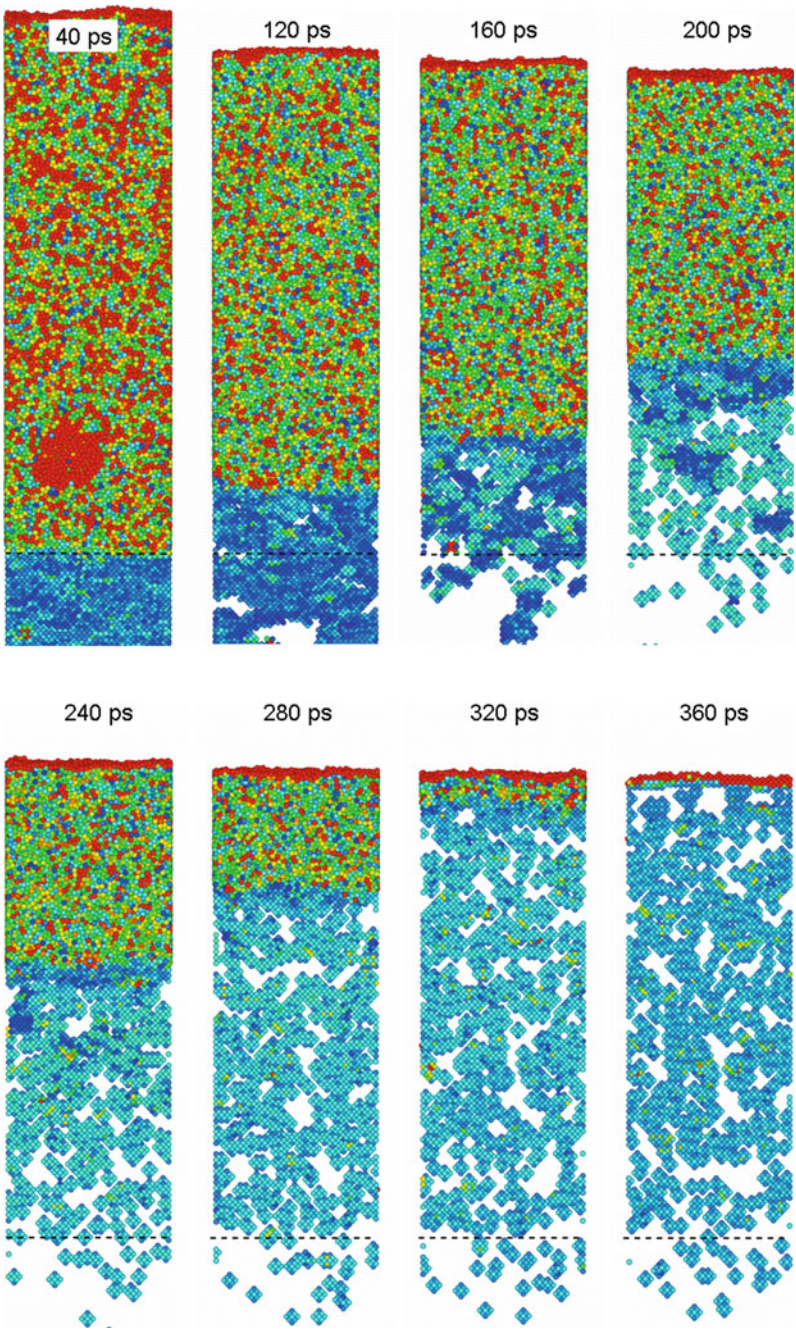
40 ps
120 ps
160 ps
200 ps
240 ps
280 ps
320 ps
360 ps

◀ **Fig. 4.2** Snapshots of atomic configurations generated in TTM–MD simulations of melting and resolidification of a bulk Cr target irradiated by a 200 fs laser pulse at an absorbed fluence of 850 J/m^2. The atomic configurations are quenched for 1 ps to reduce thermal noise in atomic positions and energies. Atoms are colored according to their potential energies and the atoms that have low potential energy and belong to local configurations with the original bcc structure are blanked to expose crystal defects. The *dashed lines* mark the maximum depth of melting reached in the simulation at about 40 ps. Each *blue ball* (a cluster of atoms with elevated energies) in the snapshots corresponds to a vacancy

mechanisms of the vacancy formation indicates that the majority of vacancies are generated at the rapidly advancing solidification front and are stabilized by the fast cooling of the surface region.

The observation of very high vacancy concentrations, up to 2–5 vacancies per 1,000 atoms, in the surface regions of the irradiated targets may have important practical implications, including the formation of nanovoids and degradation of the mechanical properties of the surface region of the target in the multi-pulse irradiation regime. The generation of vacancies, therefore, may be related to experimental observations of the incubation effect, when the laser fluence threshold for ablation/damage decreases with increasing number of laser pulses applied to the

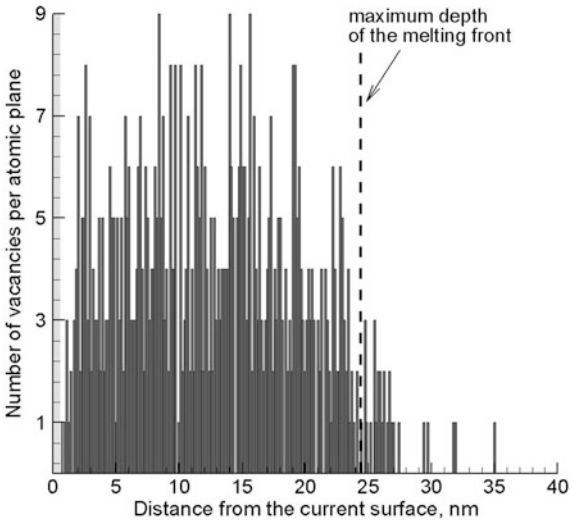

Fig. 4.3 Distribution of vacancies in the surface region of a bulk Cr target irradiated by a 200 fs laser pulse at an absorbed fluence of 850 J/m^2 at 400 ps after the laser pulse. The bars in the histogram show the number of vacancies in individual (001) atomic planes oriented parallel to the irradiated surface. The number of atoms in a defect-free (001) plane is 900. The *gray area* in the *left* part of the figure corresponds to the surface layer of the target where identification of vacancies is not possible. The *dashed line* marks the depth of the region that experiences a transient melting and resolidification during the first 330 ps of the simulation. The snapshots of atomic configurations for this simulation are shown in Fig. 4.2

same area, e.g., [149–153]. The high density of vacancies generated in the surface region may also play an important role in the redistribution of impurities or mixing/alloying in multi-component or composite targets.

To illustrate the sensitivity of the generation of crystal defects in short pulse laser processing to the crystal structure of the target material, snapshots from a simulation performed for a face-centered cubic (fcc) Ag target are shown in Fig. 4.4. In contrast to the bcc Cr target, where only a transient appearance of intrinsic stacking faults has been observed, the snapshots shown in Fig. 4.4 provide a clear view of a massive emission of partial dislocations from the melting front formed during the first tens of picoseconds after irradiation with a 100 fs laser pulse. Similarly to Fig. 4.2, the atoms that retain the original fcc local structure are blanked in Fig. 4.4 and the green planes extending down from the melted surface region correspond to low-energy stacking faults left behind by the partial dislocations (yellow lines) propagating from the melting front.

The physical conditions leading to the emission of the dislocations can be understood by considering the evolution of temperature and pressure in the irradiated target shown in Fig. 4.5a, b. In accord with the discussion of the stress confinement regime provided above, the fast energy transfer from the excited electrons to the lattice vibrations and the corresponding temperature increase in the surface region of the target (Fig. 4.5a) lead to the buildup of high compressive stresses (Fig. 4.5b). These stresses then relax by driving a compressive stress wave deeper into the bulk of the target and inducing an unloading tensile wave that forms due to the interaction of the compressive stresses with free surface of the target and follows the compressive component. The compressive and tensile components of the pressure wave leave the surface region by about 100 ps and pass through the boundary separating the MD and continuum parts of the model [154, 155] without any noticeable reflection. The onset of the emission of dislocations in the first snapshots of Fig. 4.4 coincides with the time when the tensile component of the stress wave passes through the melting front at 50–90 ps. In the single crystal fcc target oriented along $\langle 100 \rangle$ direction, the partial dislocations are activated in four different active $\{111\}$ slip planes. Interactions between the dislocations propagating along the different slip planes result in the formation of immobile dislocation segments (so-called stair-rod dislocations) that ensure stability of the dislocation configurations generated during the initial spike of temperature and thermoelastic stresses. These stable dislocation configurations remain in the target after it cools to the ambient temperature, resulting in the hardening of the laser-treated surface.

The contrast between the observation of the active emission of dislocations in the fcc Ag target and the absence of dislocations in the bcc Cr target is related to the dependence of the stress required to overcome the resistance of the crystal to the movement of dislocations (the so called Peierls stress) on the crystal structure. It is generally low in fcc crystals, where 12 close-packed $\{111\}\langle 1\bar{1}0 \rangle$ slip systems are present, but is higher in bcc crystals. Note that the generation of vacancies in the process of rapid solidification of the transiently melted surface layer, discussed above for the Cr target, is also observed in simulations performed for fcc metals.

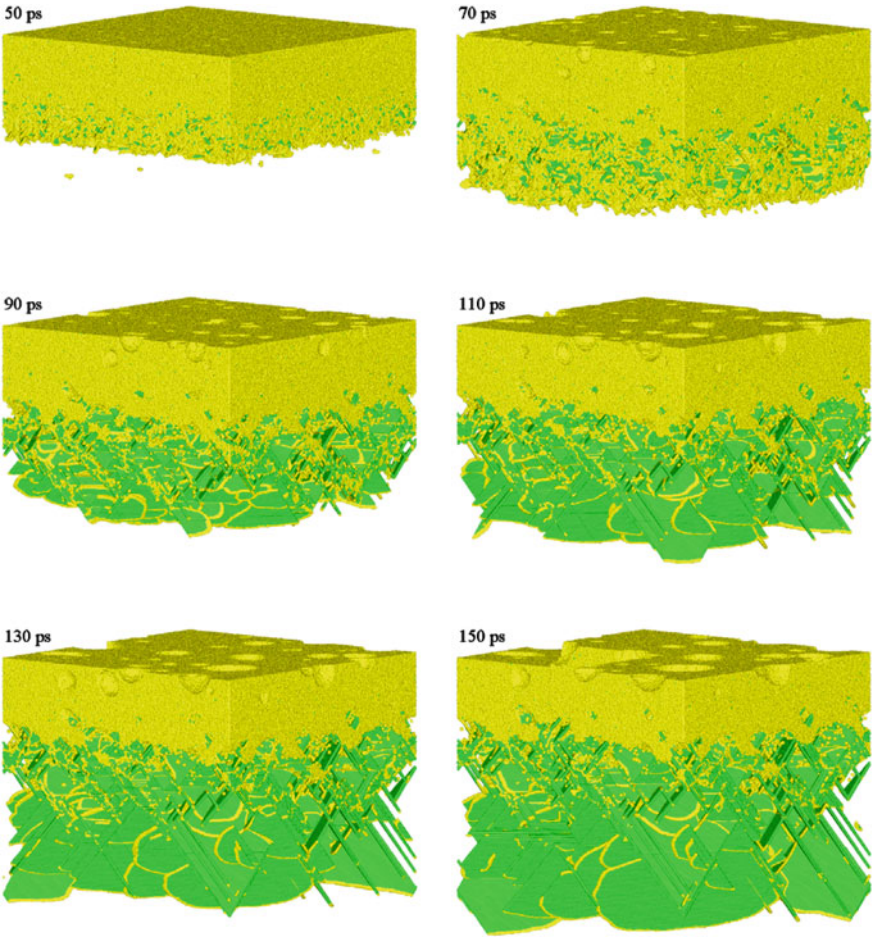

Fig. 4.4 Snapshots of atomic configurations generated in a TTM–MD simulation of a bulk Ag target irradiated by a 100 fs laser pulse at an absorbed fluence of 900 J/m^2. Only a part of the computational cell in the vicinity of the melting front (below 40 nm from the initial surface) is shown in the snapshots. The atoms are colored according to the local structure: *yellow atoms* belong to the melted part of the target or defect configurations (mostly cores of partial dislocations), *green atoms* have local hcp structure and belong to the stacking faults left behind by partial dislocations. The atoms that have local fcc structure are blanked to provide a clear view of the emission of the dislocations from the melting front. The contour plots of temperature, pressure and density evolution in this simulation are shown in Fig. 4.5

4.3.3 Photomechanical Spallation

The laser-induced stresses generated under conditions of stress confinement (see Sect. 4.3.2, Fig. 4.5b, and [45, 55, 141, 142]) can be sufficiently strong to cause mechanical fracture of a solid material or disruption and sputtering of a melted

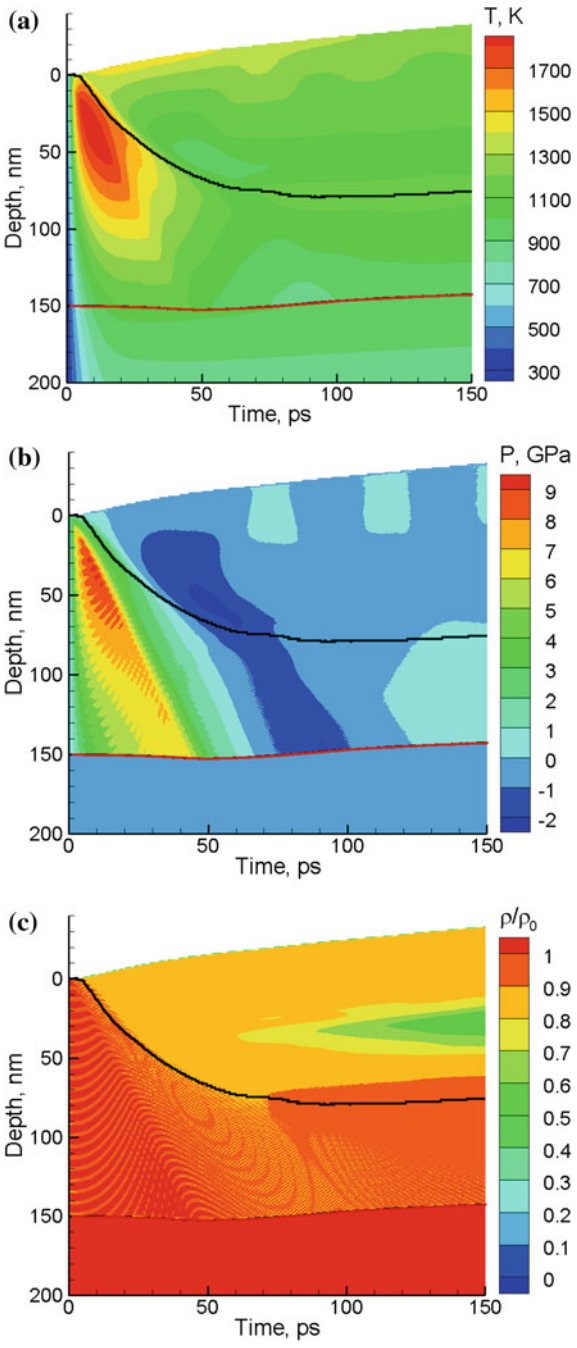

Fig. 4.5 Temperature, pressure and density contour plots in a TTM–MD simulation of a bulk Ag target irradiated by a 100 fs laser pulse at an absorbed fluence of 900 J/m^2. The density scale is normalized to the initial density before the irradiation, ρ_0. The laser pulse is directed along the Y axes from the *top* of the contour plots. The *red solid curves* separate the continuum (TTM) and atomistic (TTM–MD) parts of the computational system. The *black solid curves* separate the melted surface region from the crystalline bulk of the target. Snapshots of atomic configurations for this simulation are shown in Figs. 4.4 and 4.6b

layer. The ejection of large liquid droplets or solid particulates caused by the relaxation of the laser-induced stresses is often called photomechanical ablation or spallation [45, 52, 55, 141–145]. First MD simulations of laser spallation performed for molecular targets [52, 53, 69] revealed the dynamic process of nucleation, growth and coalescence of multiple voids in a subsurface region of the target leading to the separation and ejection of a melted layer. The results of subsequent simulations performed for metal films [40, 55, 56, 58, 90, 156] and bulk targets [45, 48, 55, 73], silicon [82], and systems with interatomic interactions described by the Lennard-Jones potential [54, 85, 157] suggest that spallation is a general process that can occur in a wide class of materials. Moreover, the void size distributions in targets as dissimilar as molecular solids [55] and metals [156] are found to follow almost identical evolution in the course of spallation, suggesting that the process of void nucleation, growth and coalescence may be similar in different materials.

The processes responsible for laser spallation are illustrated by three series of snapshots shown in Fig. 4.6 for TTM–MD simulations performed for Ag and Al targets irradiated by 100 fs laser pulses. To capture the evolution of multiple voids in the sub-surface region of the target, the simulations are performed for relatively large computational systems, where the atomistic parts of the TTM–MD model consist of 84.2 and 106.7 million atoms and have dimensions of $98.7 \times 98.7 \times 150$ nm and $93.9 \times 93.9 \times 200$ nm for the Ag and Al targets, respectively. The continuum (TTM) part of the model extends down to 4 μm in all simulations. The two simulations for the Ag target are performed at absorbed fluences of 850 and 900 J/m^2, just below and above the spallation threshold. The sharp increase of the electron–phonon coupling in Ag in the electronically excited state [118] creates the conditions for the confinement of the deposited laser energy in a relatively shallow surface region of the target, as can be seen in the temperature contour plot shown in Fig. 4.5a. The rapid heating of the lattice due to the energy transfer from the excited electrons results in the build up of high compressive stresses in the surface region of the target, as can be seen in Fig. 4.5b. The relaxation of the compressive stresses in the presence of free surface leads to the generation of an unloading tensile wave that propagates from the surface of the target and increases its strength with depth. At a certain depth under the surface the tensile stresses exceed the dynamic strength of the melted metal, leading to the generation of multiple voids. The voids can be observed at a depth of $\sim$40–60 nm in the first snapshots shown in Figs. 4.6a and 4.6b, as well as in the top parts of the snapshots shown in Fig. 4.4. The appearance of the voids is also apparent in the density contour plot shown in Fig. 4.5c, where a low density region can be seen to appear at $\sim$60 ps and expand as voids grow and coalesce. The depth of the laser-induced void nucleation and growth does not coincide with the depth where the maximum tensile stresses are generated, Fig. 4.5b. Rather, the voids are generated closer to the surface, where the ability of the melt to withstand the dynamic loading is diminished due to higher temperatures [40, 45, 48, 55].

In the simulation performed at 850 J/m^2, below the threshold for laser spallation of Ag, the growth of the voids slows down with time and turns into recession at

about 800 ps. At the same time, the fast cooling of the surface region creates conditions for fast epitaxial solidification of the melted region (see snapshot for 900 ps in Fig. 4.6a), with the velocity of the solidification front increasing with increasing undercooling. The solidification front reaches the deepest voids at about 500 ps and crosses the region where the voids are evolving during the following 1,000 ps. As a result, by the time of 1,500 ps (see the corresponding snapshot in Fig. 4.6a) all the remaining voids are trapped by the solidification front and are completely surrounded by the crystalline material. By this time, the temperature of

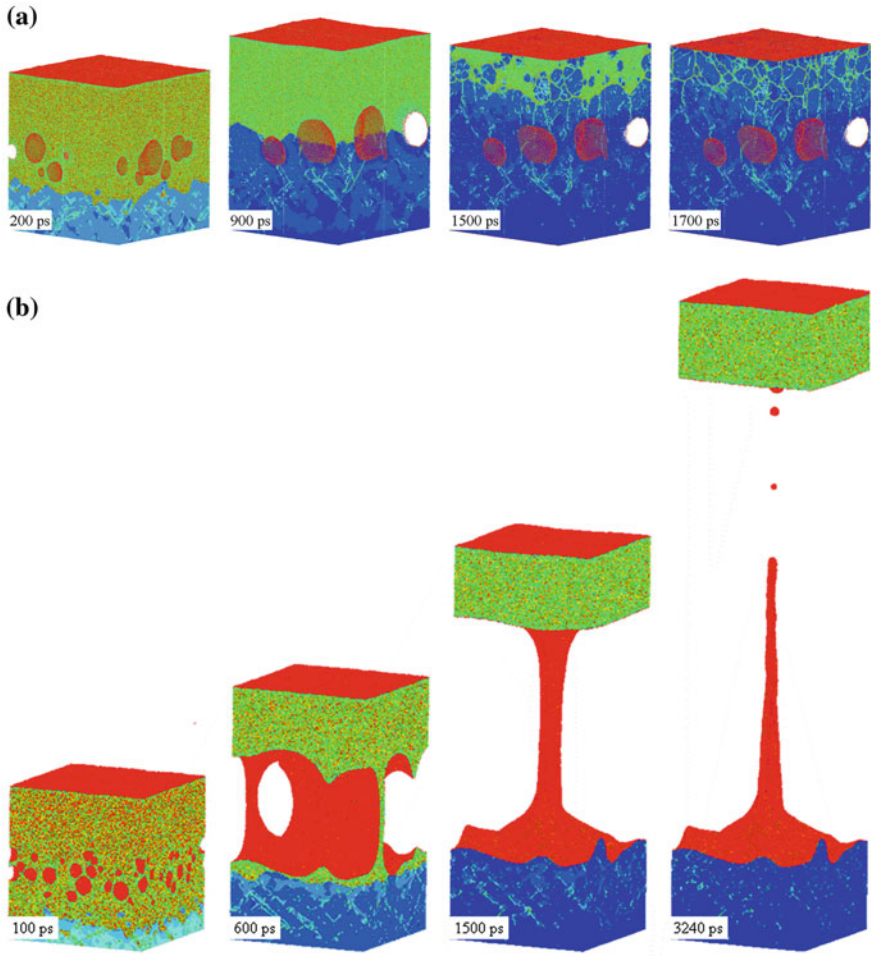

Fig. 4.6 Snapshots of atomic configurations generated in TTM–MD simulations of bulk Ag (**a**, **b**) and Al (**c**) targets irradiated by 100 fs laser pulses at absorbed fluences of 850 J/m^2 (**a**) and 900 J/m^2 (**b**, **c**). Only *top* parts of the computational cells are shown in the snapshots. The atoms are colored according to their potential energy in (**a**, **b**) and by local density of their immediate surroundings in (**c**)

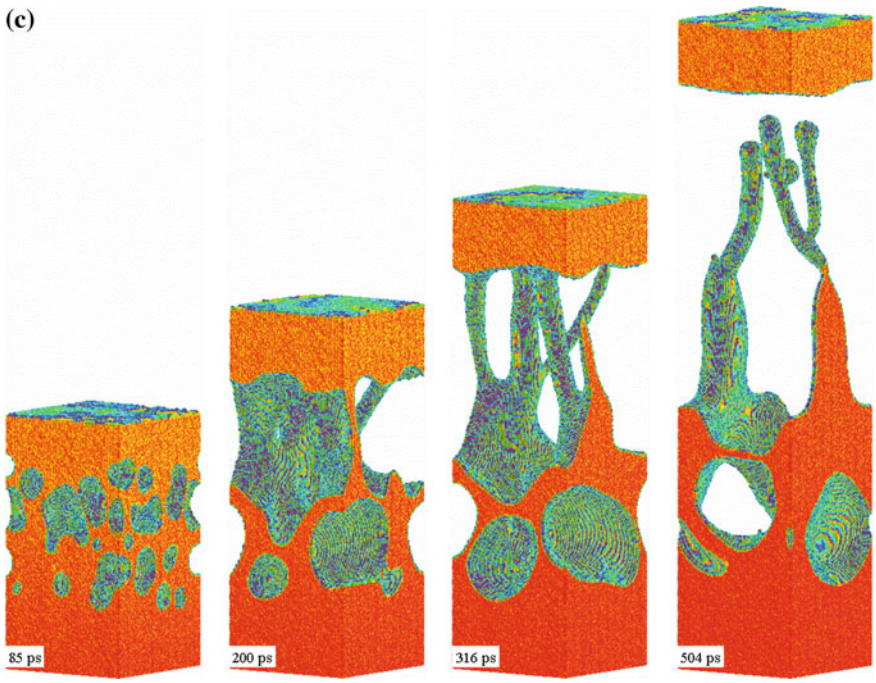

Fig. 4.6 continued

the remaining liquid layer drops down to 0.69 T_m, triggering massive homogeneous nucleation of randomly oriented crystalline regions. The homogeneous nucleation and growth of multiple crystallites result in a rapid solidification of the remaining liquid and generation of nanocrystalline structure of the top layer of the target (see snapshot for 1,700 ps in Fig. 4.6a). The voids captured by the solidification front increase the volume of the surface region, leading to an effective "swelling" of the irradiated target by about 17 nm. The computational prediction of the generation of porous structure of a surface region of the irradiated target provides a hint for explaining the recently reported experimental observation of surface swelling, or "frustrated ablation," in Al and Ag targets irradiated by 100 fs laser pulses [158]. The larger thermal conductivity and smaller melting depth near the spallation threshold in Ag, as compared to Al, make it possible to explore the swelling behavior with smaller computational systems and shorter simulation times.

In experiments, a non-uniform laser energy deposition within the laser spot and restraining effect of the cold periphery of the laser spot on the separation and ejection of the liquid layer accelerated during the initial relaxation of the laser induced stresses are likely to suppress the onset of spallation and to extend the range of laser fluences where the effect of surface swelling is observed. In the simulations, on the contrary, the use of periodic boundary conditions facilitates percolation of voids in the lateral directions and separation of the liquid layer from

the target. As a result, a relatively small increase of the laser fluence, from 850 to 900 J/m^2, leads to the ejection of a 55 nm-thick liquid layer from the Ag target, Fig. 4.6b. In this simulation, the growth and coalescence of the voids lead to the formation and eventual break down of an elongated bridge between the substrate and the top liquid layer. The expansion of the bridge hardly decelerates the layer that moves away from the target with a velocity of about 100 m/s. Although the ejected liquid layer is stabilized in the simulation by the use of the periodic boundary conditions, one can expect a rapid decomposition of the layer into liquid droplets under experimental conditions, where the variation of local fluence within the laser spot and the dynamics of the layer separation from the target are likely to cause disruption in the thin liquid shell expanding from the irradiated area of the target.

As the laser fluence increases above the spallation threshold, the size of the region affected by the void formation is increasing and the thickness of the ejected liquid layer is decreasing. These trends are illustrated in Fig. 4.6c, where snapshots are shown for a simulation performed for an Al target at a laser fluence that is about 25 % above the spallation threshold. The appearance, growth, and coalescence of voids in this case proceed at a higher temperature and lead to the formation of a complex structure of interconnected liquid regions. The top liquid layer separates from the target by 500 ps and moves away with a velocity of about 650 m/s. Although this simulation has not been continued until the complete resolidification, we can speculate that the competition between the solidification of the surface region and a relatively slow collapse/flattening of the foamy liquid structure generated in the course of spallation may be responsible for the formation of complex nanoscale surface morphology commonly observed in femtosecond laser processing experiments, e.g., [159–162].

4.3.4 Phase Explosion and Cluster Ejection

The photomechanical spallation discussed above is responsible for the onset of the collective material removal (or ablation) from the target in the regime of stress confinement. Further increase of the laser fluence above the spallation threshold results in the separation and ejection of thinner layers and/or droplets from the target and, at a sufficiently high laser fluence, induces transition to a different ablation regime commonly called the regime of "phase explosion" or "explosive boiling." In this regime, the surface region of the irradiated target is overheated above the limit of its thermodynamic stability, leading to an explosive decomposition of the overheated melted material into a mixture of vapor and liquid droplets. The transition to the regime of phase explosion is signified by an abrupt change in the composition of the ejected plume, from liquid layers and large droplets to a mixture of individual atoms, small clusters and droplets [45, 48, 52]. The sharp (threshold-like) increase in the amount of the vapor-phase atoms at the transition from photomechanical spallation to the phase explosion regime reflects

the difference in the physical mechanisms responsible for the material ejection in these two regimes. An explosive release of vapor, rather than the relaxation of photomechanical stresses, provides the main driving force for the collective ejection of the overheated surface region of the target in the regime of phase explosion.

In the ablation by longer laser pulses, in the absence of stress confinement, the spallation is not activated and the explosive boiling is the mechanism responsible for the direct transition from the regime of surface evaporation (desorption) to the collective ejection of a mixture of vapor and liquid droplets (ablation) [45, 52, 69, 74, 75, 86, 89]. Experimental observations of the existence of a threshold fluence for the onset of droplet ejection, as well as a steep increase of the rate of the material removal at the threshold, have been interpreted as evidence of the transition from normal vaporization to the phase explosion in nanosecond laser ablation [163–166].

The thermodynamic conditions leading to the onset of the phase explosion and the dependence of the ablation process on irradiation conditions and properties of the target material have been extensively investigated in MD simulations [39, 43, 45, 48, 52, 59–91]. One of the findings of the simulations is the existence of a well-defined threshold fluence for the transition from surface evaporation to the ablation regime [45, 52, 62, 69]. This threshold behavior is related to the sharp increase in the rate of homogeneous nucleation of the vapor phase in a narrow temperature range close to about 90 % of the critical temperature, which has been predicted based on the classical nucleation theory [166–169] and confirmed in simulations [45, 48, 170]. In contrast with the assumptions of the classical nucleation theory, however, the release of the vapor phase does not involve the formation of well-defined spherical bubbles but proceeds through the formation and decomposition of a transient foamy structure of interconnected liquid regions [74, 75, 86, 171]. Similarly to the fast melting at the limit of crystal stability discussed in Sect. 4.3.1, where the homogeneous melting proceeds through the collapse of the crystal structure on the picosecond timescale, there is no time for the vapor phase regions rapidly evolving in the course of the phase explosion to minimize the liquid–vapor interfacial energy and to form spherical bubbles.

The ablation dynamics in the phase explosion regime is illustrated in Fig. 4.7, where snapshots are shown for a MD simulation of laser ablation of a molecular target irradiated by a 50 ps laser pulse at an absorbed laser fluence of 80 J/m^2, which is about 2.3 times above the ablation threshold [74, 86]. Computational system used in the simulation consists of 22 million "breathing sphere" molecules (see Sect. 4.2) and has initial dimensions of 169 × 169 × 109 nm. With the optical penetration depth of 50 nm, the irradiation conditions in this simulation correspond to the absence of stress confinement and the material ejection is driven by the release of the vapor phase in the phase explosion. In the first snapshot, shown for 200 ps after the beginning of the laser pulse, one can see the expansion of the top layer of the target where the deposited energy density is sufficient to completely vaporize the material. Deeper into the target, the energy density is not high enough to vaporize the material, but is sufficient to induce an phase explosion

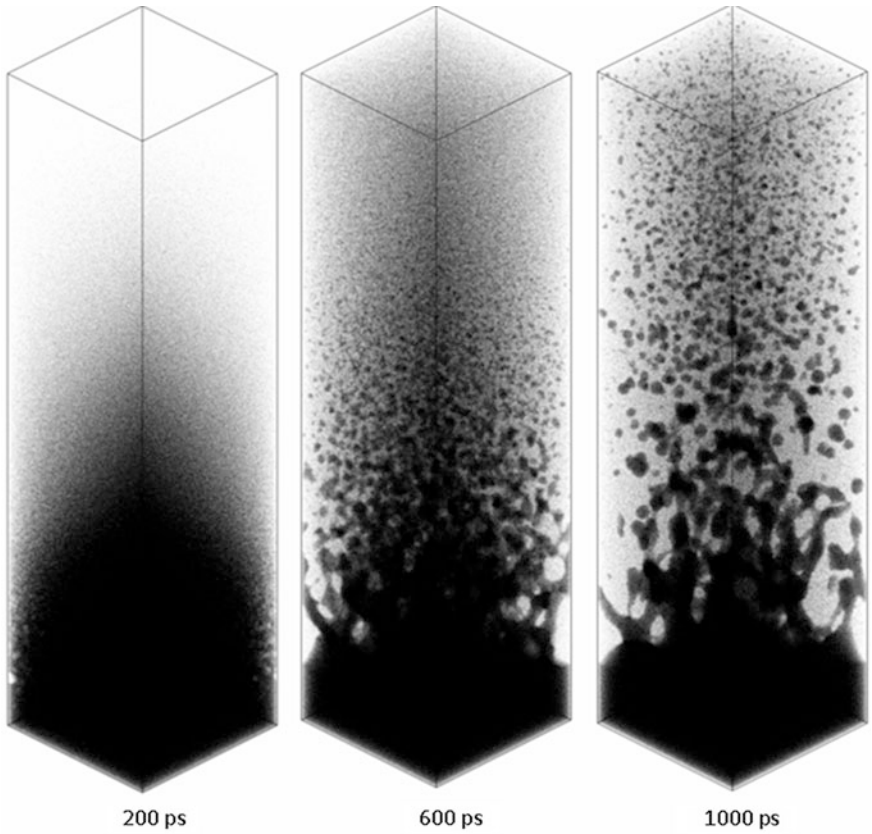

Fig. 4.7 Snapshots from a MD simulation of laser ablation of a molecular target irradiated by a 50 ps laser pulse at an absorbed fluence of 80 J/m^2. The optical penetration depth assumed in the simulation is 50 nm. Each molecule is shown as a *black dot*. Only a central part of the computational cell near the irradiated surface is shown in the snapshots

of the overheated material. The expansion of this part of the target is driven by the rapid release of vapor and proceeds through appearance of density fluctuations and formation of a transient foamy structure of interconnected liquid regions surrounded by vapor. The foamy structure eventually decomposes into individual liquid droplets, clusters and vapor-phase molecules that join the multi-component ablation plume moving away from the target (see snapshots for 600 and 1,000 ps in Fig. 4.7).

A prominent feature of the ablation process illustrated in Fig. 4.7 (and observed in MD simulations performed for different target materials, from metals to multi-component molecular systems [45, 48, 52, 74, 75, 86]) is the effect of spatial segregation of clusters/droplets of different sizes in the ablation plume. The front part of the expanding plume mostly consists of the vapor-phase molecules and small clusters, the medium size clusters are localized in the middle of the

expanding plume, and the large liquid droplets formed at the final stage of the plume development tend to be slower and are closer to the original surface. The effect of the spatial segregation of clusters/droplets of different sizes in the ablation plume has been analyzed in detail for simulations performed for molecular targets with both long (no stress confinement) [74] and short (stress confinement) [172] laser pulses and has been shown to be defined by the variation of the mechanisms of the cluster formation with the depth of origin (and the energy density deposited by the laser pulse) of the material contributing to different parts of the ablation plume. The cluster segregation effect, predicted in the simulations, can be related to the results of plume imaging experiments [173–177], where splitting of the plume into a fast component with optical emission characteristic for neutral atoms and a slow component with blackbody-like emission attributed to the presence of hot clusters [178] is observed. Similarly, and consistently with the results of the simulations discussed above, a layered structure of the plume (vaporized layer followed by small particles and larger droplets) observed in nanosecond laser ablation of water and soft tissue [179] is attributed to the succession of phase transitions occurring at different depth in the irradiated target [179, 180].

An interesting observation in the simulations is that the larger droplets in the plume tend to have substantially higher internal temperatures as compared to the smaller droplets and clusters [74, 172]. Given that the larger droplets are ejected from deeper parts of the target, where the energy density deposited by the laser pulse is smaller, this observation is surprising from the first sight and calls for analogy with so-called Mpemba effect named after a secondary school student in Tanzania who observed that hot milk freezes faster than cold milk when placed into a refrigerator at the same time [181]. Similarly to the Mpemba effect, different pathways of the thermal energy dissipation are activated at different levels of the initial thermal energy, leading to the faster cooling of the parts of the plume where the initial overheating is higher. In particular, the stronger overheating of the upper part of the ablation plume leads to a more vigorous phase explosion with a larger fraction of the released vapor-phase molecules, a faster expansion, and a more efficient cooling, as compared to a slower evaporative cooling of the large droplets ejected in the tail of the plume.

4.3.5 Matrix-Assisted Pulsed Laser Evaporation

In the previous sections, the mechanisms of laser spallation and ablation are discussed for one-component metals and molecular targets. Many systems of practical importance, however, have a more complex composite structure and/or consist of multiple components. Molecular dynamics technique describes material with atomic- or molecular-level resolution and, therefore, the extension of this technique to investigation of laser interactions with multi-component targets of arbitrary structural complexity is relatively straightforward. Recent computational study of laser interactions with frozen dilute polymer solutions [72, 86, 87, 103,

104, 171] provides an example of adopting the MD model for multi-component molecular targets. This study was motivated by the need for understanding the mechanisms of molecular transport in matrix-assisted pulsed laser evaporation (MAPLE) technique for deposition of polymer and nanocomposite thin films [182, 183] and, in particular, the origin of unexpectedly large roughness of the films deposited by MAPLE [87, 103, 104, 184–193]. The simulations reveal that, contrary to the original picture of the ejection and transport of individual polymer molecules [182, 183], the deposition of polymer films is only possible in the ablation regime, when the polymer molecules are ejected as parts of polymer-matrix clusters/droplets generated in the process of the explosive disintegration of the overheated matrix [86]. The entanglement of the polymer molecules is found to facilitate the formation of intricate elongated viscous droplets that can be related to the "nanofiber" or "necklace" polymer features observed in SEM images of films deposited by MAPLE [103, 104, 186]. Moreover, in-flight molecular rearrangements in the ejected polymer-matrix droplets [87] and the dynamic processes occurring upon landing of the droplets on a substrate [104] have been connected to the formation of characteristic surface features observed in MAPLE experiments, such as wrinkled "deflated balloons," "collapsed pipes," and interconnected polymer filaments [87, 104, 186, 188–190].

The simulations of MAPLE has been recently extended to targets loaded with carbon nanotubes (CNTs) [171] and the ability of the MAPLE technique to transfer large structural elements that may be required for deposition of nanostructured films and coatings has been demonstrated. To enable the investigation of the mechanisms of the ejection and transfer of CNTs in MAPLE, the coarse-grained model for laser interactions with molecular systems has been integrated with a mesoscopic dynamic model recently developed for CNTs [194–196]. The model represents each individual CNT as a sequence of stretchable cylindrical segments. The dynamic behavior of CNTs is governed by a mesoscopic force field that accounts for the internal stretching, bending, and buckling of nanotubes as well as for the van der Waals interactions among the CNTs. The simulations performed for MAPLE targets loaded with CNTs of different length (from 16 to 150 nm) and at different CNT concentrations (from 1 to 17 wt %) demonstrate that, similarly to MAPLE of polymer molecules [86], the ejection CNTs is driven by the explosive boiling of the overheated matrix. The CNTs with length comparable to or even exceeding the laser penetration depth can be efficiently entrained in the expanding matrix plume, lifted off from the target, and transferred to the substrate. Moreover, the ejection of CNT bundles and large tangles has been observed in simulations performed for targets containing networks of interconnected CNT bundles.

The dynamics of disintegration of the network structures driven by the explosive boiling of the matrix material is illustrated in snapshots shown in Fig. 4.8. The MAPLE target used in this simulation is composed of a network of bundles consisting of more than a thousand of 150-nm long (10, 10) single-walled CNTs immersed into a frozen matrix represented by about 20 million molecules. The simulation is performed at the same laser fluence of 80 J/m^2 that is used in the

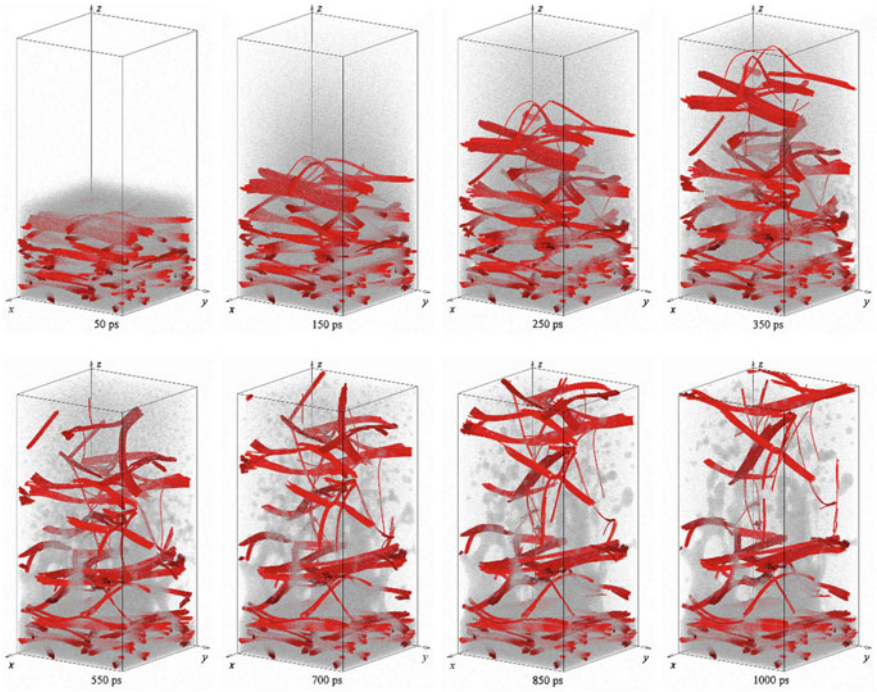

Fig. 4.8 Snapshots from a MD simulation of the ejection of CNTs from a MAPLE target loaded with 17 wt % of 150 nm long CNTs and irradiated by a 50 ps laser pulse at an absorbed fluence of 80 J/m^2. The CNTs in the target are arranged into a continuous network of bundles that is embedded into a frozen matrix. The nanotubes are shown as *red* cylinders and the matrix molecules are shown as small *gray dots*. This and other simulations of MAPLE of CNTs are discussed in [171]

simulation of laser ablation of one-component molecular matrix illustrated in Fig. 4.7. The visual picture of the explosive boiling of the overheated matrix, leading to the formation and disintegration of a transient foamy structure of interconnected liquid regions, is similar in the two simulations. The rapid expansion of the matrix plume in the simulation illustrated in Fig. 4.8 entrains the CNT bundles and tears several large CNT tangles out of the continuous network. The mass of the largest CNT tangle ejected in the simulation exceeds 50 MDa (not counting the mass of the attached matrix molecules), even though the simulation is performed for a relatively short laser penetration depth of 50 nm. No signs of any significant splitting or thinning of the thick bundles present in the initial network structure is observed in the simulation, suggesting that large fragments of the network ejected from the target can be expected to be transported to the substrate. This computational prediction is consistent with experimental observations of MAPLE deposition of CNT bundles and agglomerates with sizes comparable to or exceeding the laser penetration depth in the target [186, 197, 198]. The survival of large CNT structures held together by relatively weak van der Waals forces

suggests that fragile structural elements or molecular agglomerates with complex secondary structures can be transferred and deposited to the substrate with the MAPLE technique.

4.4 Concluding Remarks and Future Directions

The development of several computational approaches for the description of laser coupling and relaxation of photo-excited states in metals, semiconductors, insulators and molecular systems within the general framework of the classical MD technique, combined with the fast growth of the available computing resources, puts MD modeling at the forefront of computational investigation of laser-materials interactions. The examples of recent applications of MD technique to investigation of laser melting, generation of crystal defects, photomechanical spallation, explosive boiling and molecular entrainment in laser ablation, briefly reviewed in this chapter, demonstrate the ability of atomic/molecular-level simulations to provide insights into the mechanisms of laser-materials interactions, to assist in interpretation of experimental observations, and to clarify some of the research questions of direct relevance to practical applications. Clear visual representations of laser-induced dynamic processes provided by series of snapshots taken at different moments during the simulations [199] is a bonus feature of MD simulations that offers a path towards the development of an intuitive picture of the complex phenomenon of laser-materials interactions.

Future progress in atomistic simulations of laser-materials interactions is likely to take advantage of the ability of massively parallel simulations to model increasingly large systems (hundreds of nanometers or 10^8–10^9 atoms) for longer simulation times (tens of nanoseconds), thus approaching the experimental time- and length-scales of processes induced by laser energy deposition. The increased accuracy of interatomic potentials in the description of phase transformations and material properties under conditions of high temperature and high pressure, characteristic of laser-materials interactions, is likely to enable material-specific computational predictions that can be quantitatively related to experimental data. The design of novel mesoscopic dynamic models may result in expansion of the domain of applicability of the MD-type coarse-grained dynamic simulations into the area of laser interactions with complex multi-phase and multi-component systems, such as nanocomposite materials and biological tissue.

Finally, MD simulations can play a key role in the design of an integrated multiscale computational model capable of accounting for interrelations between processes occurring at different time- and length-scales and providing a comprehensive picture of laser-materials interactions. In particular, classical MD simulations can serve as a bridge between the ab initio electronic structure calculations, which reveal the transient changes in the interatomic bonding and the ultrafast atomic dynamics in the electronically excited states, and continuum-level modeling of the effective (macroscopic) material response to the laser excitation.

To enable the incorporation of the predictions of ab initio calculations into the framework of MD simulations, new computational methods should be developed for the description of changes in the interatomic interactions due to the electronic excitations, as well as modification of the thermophysical and transport properties of materials in electronically excited states. Recent work in this direction includes incorporation of the contribution of so-called electron pressure [200] exerted on atoms due to the sharp electron temperature gradient generated by femtosecond laser irradiation of metals into the TTM–MD model [201–204] and the design of electron temperature dependent interatomic potentials for Si [205–207] and W [208] based on ab initio calculations performed at different levels of electronic excitation. The electron temperature dependences of the thermophysical material properties (electron–phonon coupling factor, electron heat capacity, and heat conductivity) [118], revealed in the computational analysis based on first-principles electronic structure calculations of the electron density of states, have been incorporated in the TTM–MD model and resulted in an improved agreement between the computational predictions and experimental observations [47, 132, 209, 210].

Further advancements of computational models are needed to achieve more accurate representation of the material behavior and properties in the electronically excited state in MD simulations. In particular, the uncertainty in the contribution of non-equilibrium electrons to the initial ultra-fast energy redistribution, inherent to the TTM–MD model (e.g., see discussion of the ballistic energy transport in [46, 51, 211, 212]), may be resolved by adding spatial dependence to the kinetic approaches based on the solution of the Boltzmann equation for electrons [213, 214] or Monte-Carlo treatment of individual photo-excitation and scattering events [215] and incorporating these approaches into MD models. The effect of the electronic excitation in metals cannot be entirely described by the introduction of electron pressure and additional modifications of the effective interatomic interactions should be introduced to match the predictions of ab initio calculations and experimental probing. Similarly, it may be difficult to design an adequate description of the effect of laser excitation on interatomic bonding in semiconductors and dielectrics based solely on the concept of electronic temperature, making it necessary to consider local changes in interatomic bonding in the vicinity of the optically excited states, particularly at low excitation densities.

The extension of the integrated multiscale computational approach to larger time- and length-scales that are beyond the reach of atomistic modeling can be achieved by using the detailed information on laser-induced structural and phase transformations, revealed in MD simulations, in the design of continuum-level models. The continuum modeling of laser-materials interactions have to include assumptions on the kinetics of phase transformations far from equilibrium, evolution of photomechanical damage under the action of laser-induced tensile stresses, characteristics of the ablation plume generated as a result of the explosive decomposition of the overheated surface region in laser ablation, etc. The results of MD simulations can be formulated in terms of the thermodynamic parameters such as pressure, temperature, and density distributions, as well as the structural/

phase transformations in the material, and can be used to provide the necessary information for a reliable description of fast nonequilibrium processes within a continuum model. The information on the kinetics of the homogeneous and heterogeneous melting processes [41, 44, 45, 47, 136], evolution of void size distribution in laser spallation [55, 156], and the cluster size distributions in the ablation plume [74, 86, 174] can provide ideas for the design of new constitutive relations for continuum modeling of the material behavior under conditions of rapid temperature variations and ultrafast mechanical loading realized in short-pulse laser processing.

The parameters of the ablation plume (velocity, spatial and size distributions of the ejected atoms/molecules, clusters, and droplets) predicted in MD simulations can also be used as initial conditions in the direct simulation Monte Carlo (DSMC) method [216] capable of following the evolution of the ablation plume on the time- and length-scales characteristic for experimental conditions, up to hundreds of microseconds and millimeters [217–225]. First applications of the combined MD-DSMC model for simulation of laser interactions with molecular systems [75, 174, 226–228] have demonstrated the ability of the model to reveal connections between the processes occurring at the initial stage of the plume formation and during the long-term plume expansion. In particular, the initial generation of clusters in the phase explosion, predicted in MD simulations, is found to provide cluster precursors for condensation during the long-term plume expansion, thus eliminating the three-body collision bottleneck in the cluster growth process. The presence of clusters facilitates the collisional condensation and evaporation processes, thus affecting the cluster composition of the plume as well as the overall dynamics of the plume expansion.

Acknowledgments The authors acknowledge financial support provided by the National Science Foundation (USA) through Grants DMR-0907247, CBET-1033919, and CMMI-1301298 and by the Air Force Office of Scientific Research through Grant FA9550-10-1-0541. Computational support was provided by the Oak Ridge Leadership Computing Facility (projects MAT009 and MAT048) and the National Science Foundation through the Extreme Science and Engineering Discovery Environment (projects TG-DMR110090 and TG-DMR130010).

References

1. V. Recoules, J. Clérouin, G. Zérah, P.M. Anglade, S. Mazevet, Phys. Rev. Lett. **96**, 055503 (2006)
2. F. Bottin, G. Zérah, Phys. Rev. B **75**, 174114 (2007)
3. P.B. Hillyard, D.A. Reis, K.J. Gaffney, Phys. Rev. B **77**, 195213 (2008)
4. P.L. Silvestrelli, A. Alavi, M. Parrinello, D. Frenkel, Phys. Rev. Lett. **77**, 3149–3152 (1996)
5. J.S. Graves, R.E. Allen, Phys. Rev. B **58**, 13627 (1998)
6. H.O. Jeschke, M.E. Garcia, in *Chapter 7 Nonlinear Optics, Quantum Optics, and Ultrafast Phenomena with X-Rays*, ed. by B.W. Adams (Springer, New York, 2003), pp. 175–214
7. T. Dumitrica, A. Burzo, Y. Dou, R.E. Allen, Phys. Status Solidi B **241**, 2331–2342 (2004)
8. H.O. Jeschke, M.S. Diakhate, M.E. Garcia, Appl. Phys. A **96**, 33–42 (2009)

9. B.R. Torralva, R.E. Allen, J. Mod. Opt. **49**, 593–625 (2002)
10. Y. Dou, B.R. Torralva, R.E. Allen, Chem. Phys. Lett. **392**, 352–357 (2004)
11. H.O. Jeschke, M.E. Garcia, M. Lenzner, J. Bonse, J. Krüger, W. Kautek, Appl. Surf. Sci. **197–198**, 839–844 (2002)
12. Z. Lin, R.E. Allen, J. Phys.: Condens. Matter **21**, 485503 (2009)
13. A.J. Neukirch, Z.Y. Guo, O.V. Prezhdo, J. Phys. Chem. C **116**, 15034–15040 (2012)
14. R.K. Singh, J. Narayan, Phys. Rev. B **41**, 8843–8858 (1990)
15. A. Peterlongo, A. Miotello, R. Kelly, Phys. Rev. E **50**, 4716–4727 (1994)
16. J.R. Ho, C.P. Grigoropoulos, J.A.C. Humphrey, J. Appl. Phys. **78**, 4696–4709 (1995)
17. X. Xu, G. Chen, K.H. Song, Int. J. Heat Mass Transfer **42**, 1371–1382 (1999)
18. V.A. Gnatyuk, T. Aoki, O.S. Gorodnychenko, Y. Hatanaka, Appl. Phys. Lett. **83**, 3704–3706 (2003)
19. I.H. Chowdhury, X. Xu, Num. Heat Transfer A **44**, 219–232 (2003)
20. A. Bogaerts, Z. Chen, R. Gijbels, A. Vertes, Spectrochim. Acta B **58**, 1867–1893 (2003)
21. N. Bityurin, B.S. Luk'yanchuk, M.H. Hong, T.C. Chong, Chem. Rev. **103**, 519–552 (2003)
22. K.N. Vonatsos, D.I. Pantelis, Appl. Phys. A **80**, 885–889 (2005)
23. O.A. Bulgakova, N.M. Bulgakova, V.P. Zhukov, Appl. Phys. A **101**, 53–59 (2010)
24. N.M. Bulgakova, R. Stoian, A. Rosenfeld, I.V. Hertel, in *Chapter 4 in Laser-Surface Interactions for New Materials Production: Tailoring Structure and Properties*, vol. 130, Springer Series in Materials Science, ed. by A. Miotello, P.M. Ossi (Springer, New York, 2010), pp. 81–97
25. K. Eidmann, J. Meyer-ter-Vehn, T. Schlegel, S. Huller, Phys. Rev. E **62**, 1202–1214 (2000)
26. Y. Kondoh, T. Yabe, J. Maehara, T. Nakamura, Y. Ogata, Phys. Rev. E **68**, 066408 (2003)
27. F. Vidal, T.W. Johnston, J.-C. Kieffer, F. Martin, Phys. Rev. B **70**, 184125 (2004)
28. J.P. Colombier, P. Combis, F. Bonneau, R. Le Harzic, E. Audouard, Phys. Rev. B **71**, 165406 (2005)
29. M.E. Povarnitsyn, T.E. Itina, M. Sentis, K.V. Khishchenko, P.R. Levashov, Phys. Rev. B **75**, 235414 (2007)
30. A.N. Volkov, L.V. Zhigilei, J. Phys.: Conf. Ser. **59**, 640–645 (2007)
31. A.N. Volkov, C. Sevilla, L.V. Zhigilei, Appl. Surf. Sci. **253**, 6394–6399 (2007)
32. M.E. Povarnitsyn, T.E. Itina, K.V. Khishchenko, P.R. Levashov, Phys. Rev. Lett. **103**, 195002 (2009)
33. J.P. Colombier, P. Combis, E. Audouard, R. Stoian, New J. Phys. **14**, 013039 (2012)
34. M.P. Allen, D.J. Tildesley, *Computer Simulation of Liquids* (Clarendon Press, Oxford, 1987, 1990)
35. D. Frenkel, B. Smit, *Understanding molecular simulation: from algorithms to applications* (Academic Press, San Diego, 1996)
36. L.V. Zhigilei, Z. Lin, D.S. Ivanov, E. Leveugle, D.H. Duff, D. Thomas, C. Sevilla, S.J. Guy, in *Chapter 3 in Laser-Surface Interactions for New Materials Production: Tailoring Structure and Properties*, vol. 130, Springer Series in Materials Science, ed. by A. Miotello, P.M. Ossi (Springer, New York, 2010), pp. 43–79
37. C.F. Richardson, P. Clancy, Mol. Sim. **7**, 335–355 (1991)
38. H. Hakkinen, U. Landman, Phys. Rev. Lett. **71**, 1023–1026 (1993)
39. X. Wang, X. Xu, J. Heat Transfer **124**, 265–274 (2002)
40. D.S. Ivanov, L.V. Zhigilei, Phys. Rev. B **68**, 064114 (2003)
41. D.S. Ivanov, L.V. Zhigilei, Phys. Rev. Lett. **91**, 105701 (2003)
42. D.S. Ivanov, L.V. Zhigilei, Appl. Phys. A **79**, 977–981 (2004)
43. X. Wang, Y. Lu, J. Appl. Phys. **98**, 114304 (2005)
44. Z. Lin, L.V. Zhigilei, Phys. Rev. B **73**, 184113 (2006)
45. L.V. Zhigilei, Z. Lin, D.S. Ivanov, J. Phys. Chem. C **113**, 11892–11906 (2009)
46. D.A. Thomas, Z. Lin, L.V. Zhigilei, E.L. Gurevich, S. Kittel, R. Hergenröder, Appl. Surf. Sci. **255**, 9605–9612 (2009)
47. Z. Lin, E.M. Bringa, E. Leveugle, L.V. Zhigilei, J. Phys. Chem. C **114**, 5686–5699 (2010)
48. E.T. Karim, Z. Lin, L.V. Zhigilei, AIP Conf. Proc. **1464**, 280–293 (2012)

49. Z. Lin, R.A. Johnson, L.V. Zhigilei, Phys. Rev. B **77**, 214108 (2008)
50. D.S. Ivanov, Z. Lin, B. Rethfeld, G.M. O'Connor, T.J. Glynn, L.V. Zhigilei, J. Appl. Phys. **107**, 013519 (2010)
51. C. Wu, D.A. Thomas, Z. Lin, L.V. Zhigilei, Appl. Phys. A **104**, 781–792 (2011)
52. L.V. Zhigilei, B.J. Garrison, J. Appl. Phys. **88**, 1281–1298 (2000)
53. A.G. Zhidkov, L.V. Zhigilei, A. Sasaki, T. Tajima, Appl. Phys. A **73**, 741–747 (2001)
54. S.I. Anisimov, V.V. Zhakhovskii, N.A. Inogamov, K. Nishihara, A M. Oparin, Yu.V. Petrov, Pis'ma Zh. Eksp. Teor. Fiz. **77**, 731 (2003) [JETP Lett. **77**, 606–610 (2003)]
55. E. Leveugle, D.S. Ivanov, L.V. Zhigilei, Appl. Phys. A **79**, 1643–1655 (2004)
56. A.K. Upadhyay, H.M. Urbassek, J. Phys. D **38**, 2933–2941 (2005)
57. H.Y. Lai, P.H. Huang, Appl. Surf. Sci. **254**, 3067–3073 (2008)
58. B.J. Demaske, V.V. Zhakhovsky, N.A. Inogamov, I.I. Oleynik, Phys. Rev. B **82**, 064113 (2010)
59. E. Ohmura, I. Fukumoto, Int. J. Japan Soc. Prec. Eng. **30**, 128–133 (1996)
60. L.V. Zhigilei, P.B.S. Kodali, B.J. Garrison, J. Phys. Chem. B **101**, 2028–2037 (1997)
61. L.V. Zhigilei, B.J. Garrison, Appl. Phys. Lett. **71**, 551–553 (1997)
62. L.V. Zhigilei, P.B.S. Kodali, B.J. Garrison, Chem. Phys. Lett. **276**, 269–273 (1997)
63. E. Ohmura, I. Fukumoto, I. Miyamoto, Int. J. Japan Soc. Prec. Eng. **32**, 248–253 (1998)
64. R.F.W. Herrmann, J. Gerlach, E.E.B. Campbell, Appl. Phys. A **66**, 35–42 (1998)
65. X. Wu, M. Sadeghi, A. Vertes, J. Phys. Chem. B **102**, 4770–4778 (1998)
66. L.V. Zhigilei, P.B.S. Kodali, B.J. Garrison, J. Phys. Chem. B **102**, 2845–2853 (1998)
67. L.V. Zhigilei, B.J. Garrison, Rapid Commun. Mass Spectrom. **12**, 1273–1277 (1998)
68. L.V. Zhigilei, B.J. Garrison, Appl. Phys. Lett. **74**, 1341–1343 (1999)
69. L.V. Zhigilei, B.J. Garrison, Appl. Phys. A **69**, S75–S80 (1999)
70. Y.G. Yingling, L.V. Zhigilei, B.J. Garrison, J. Photochem. Photobiol. A **145**, 173–181 (2001)
71. S. Kristyan, A. Bensura, A. Vertes, Theor. Chem. Acc. **107**, 319–325 (2002)
72. T.E. Itina, L.V. Zhigilei, B.J. Garrison, J. Phys. Chem. B **106**, 303–310 (2002)
73. C. Schäfer, H.M. Urbassek, L.V. Zhigilei, Phys. Rev. B **66**, 115404 (2002)
74. L.V. Zhigilei, Appl. Phys. A **76**, 339–350 (2003)
75. L.V. Zhigilei, E. Leveugle, B.J. Garrison, Y.G. Yingling, M.I. Zeifman, Chem. Rev. **103**, 321–347 (2003)
76. P. Lorazo, L.J. Lewis, M. Meunier, Phys. Rev. Lett. **91**, 225502 (2003)
77. N.N. Nedialkov, P.A. Atanasov, S.E. Imamova, A. Ruf, P. Berger, F. Dausinger, Appl. Phys. A **79**, 1121–1125 (2004)
78. X. Xu, C. Cheng, I.H. Chowdhury, ASME Trans. J. Heat Transfer **126**, 727–734 (2004)
79. C. Cheng, X. Xu, Phys. Rev. B **72**, 165415 (2005)
80. X.W. Wang, J. Phys. D **38**, 1805–1823 (2005)
81. Y.G. Yingling, B.J. Garrison, J. Phys. Chem. B **109**, 16482–16489 (2005)
82. P. Lorazo, L.J. Lewis, M. Meunier, Phys. Rev. B **73**, 134108 (2006)
83. N.N. Nedialkov, P.A. Atanasov, Appl. Surf. Sci. **252**, 4411–4415 (2006)
84. S.I. Anisimov, V.V. Zhakhovskii, N.A. Inogamov, K. Nishihara, YuV Petrov, V.A. Khokhlov, J. Exp. Theor. Phys. **103**, 183–197 (2006)
85. M.B. Agranat, S.I. Anisimov, S.I. Ashitkov, V.V. Zhakhovskii, N.A. Inogamov, K. Nishihara, YuV Petrov, V.E. Fortov, V.A. Khokhlov, Appl. Surf. Sci. **253**, 6276–6282 (2007)
86. E. Leveugle, L.V. Zhigilei, J. Appl. Phys. **102**, 074914 (2007)
87. E. Leveugle, A. Sellinger, J.M. Fitz-Gerald, L.V. Zhigilei, Phys. Rev. Lett. **98**, 216101 (2007)
88. M. Prasad, P. Conforti, B.J. Garrison, J. Appl. Phys. **101**, 103113 (2007)
89. L. Zhang, X. Wang, Appl. Surf. Sci. **255**, 3097–3103 (2008)
90. M. Gill-Comeau, L.J. Lewis, Phys. Rev. B **84**, 224110 (2011)
91. X. Li, L. Jiang, Appl. Phys. A **109**, 367–376 (2012)
92. B.J. Garrison, D. Srivastava, Annu. Rev. Phys. Chem. **46**, 373–394 (1995)

93. A.F. Voter, MRS Bull. **21**, 17–18 (1996)
94. S.B. Sinnott, D.W. Brenner, MRS Bull. **37**, 469–473 (2012)
95. S.L. Johnson, M.R. Papantonakis, R.F. Haglund, in *Chapter 8 in Laser-Surface Interactions for New Materials Production: Tailoring Structure and Properties*, vol. 130, Springer Series in Materials Science, ed. by A. Miotello, P.M. Ossi (Springer, New York, 2010), pp. 177–202
96. R.E. Wyatt, C. Iung, C. Leforestier, Acc. Chem. Res. **28**, 423–429 (1995)
97. V. Kozich, W. Werncke, J. Dreyer, K.-W. Brzezinka, M. Rini, A. Kummrow, T. Elsaesser, J. Chem. Phys. **117**, 719–726 (2002)
98. H. Kim, D.D. Dlott, Y. Won, J. Chem. Phys. **102**, 5480–5485 (1995)
99. J.C. Deàk, L.K. Iwaki, S.T. Rhea, D.D. Dlott, J. Raman Spectr. **31**, 263–274 (2000)
100. E.L. Sibert, R. Rey, J. Chem. Phys. **116**, 237–257 (2002)
101. M. Sadeghi, X. Wu, A. Vertes, J. Phys. Chem. B **105**, 2578–2587 (2001)
102. Ł. Dutkiewicz, R.E. Johnson, A. Vertes, R. Pędrys, J. Phys. Chem. A **103**, 2925–2933 (1999)
103. E. Leveugle, L.V. Zhigilei, A. Sellinger, J.M. Fitz-Gerald, Appl. Surf. Sci. **253**, 6456–6460 (2007)
104. A. Sellinger, E. Leveugle, J.M. Fitz-Gerald, L.V. Zhigilei, Appl. Phys. A **92**, 821–829 (2008)
105. R. Knochenmuss, L.V. Zhigilei, J. Phys. Chem. B **109**, 22947–22957 (2005)
106. R. Knochenmuss, L.V. Zhigilei, J. Mass Spectrom. **45**, 333–346 (2010)
107. R. Knochenmuss, L.V. Zhigilei, Anal. Bioanal. Chem. **402**, 2511–2519 (2012)
108. B.J. Garrison, R. Srinivasan, J. Appl. Phys. **57**, 2909–2914 (1985)
109. B.J. Garrison, R. Srinivasan, Appl. Phys. Lett. **44**, 849–851 (1984)
110. Y.G. Yingling, B.J. Garrison, J. Phys. Chem. B **108**, 1815–1821 (2004)
111. Y. Dou, L.V. Zhigilei, N. Winograd, B.J. Garrison, J. Phys. Chem. A **105**, 2748–2755 (2001)
112. Y. Dou, L.V. Zhigilei, Z. Postawa, N. Winograd, B.J. Garrison, Nucl. Instr. Meth. B **180**, 105–111 (2001)
113. Y. Dou, N. Winograd, B.J. Garrison, L.V. Zhigilei, J. Phys. Chem. B **107**, 2362–2365 (2003)
114. K.M. Smith, M.Y. Hussaini, L.D. Gelb, S.D. Allen, Appl. Phys. A **77**, 877–882 (2003)
115. X. Gu, H.M. Urbassek, Appl. Phys. B **81**, 675–679 (2005)
116. X. Gu, H.M. Urbassek, Appl. Surf. Sci. **253**, 4142–4149 (2007)
117. O. Stein, Z. Lin, L.V. Zhigilei, M. Asscher, J. Phys. Chem. A **115**, 6250–6259 (2011)
118. Z. Lin, L.V. Zhigilei, V. Celli, Phys. Rev. B **77**, 075133 (2008)
119. F. Gao, D.J. Bacon, P.E.J. Flewitt, T.A. Lewis, Modelling Simul. Mater. Sci. Eng. **6**, 543–556 (1998)
120. D.M. Duffy, A.M. Rutherford, T. Phys. Cond. Matter **19**, 016207 (2007)
121. J.D. Schall, C.W. Padgett, D.W. Brenner, Mol. Simulat. **31**, 283–288 (2005)
122. S.I. Anisimov, B.L. Kapeliovich, T.L. Perel'man, Sov. Phys. JETP **39**, 375–377 (1974)
123. R. Holenstein, S.E. Kirkwood, Y.Y. Tsui, R. Fedosejevs, Proc. SPIE **5579**, 688–695 (2004)
124. Y. Wang, X. Xu, L. Zheng, Appl. Phys. A **92**, 849–852 (2008)
125. Y. Cherednikov, N.A. Inogamov, H.M. Urbassek, J. Opt. Soc. Am. B **28**, 1817–1824 (2011)
126. S. Williamson, G. Mourou, J.C.M. Li, Phys. Rev. Lett. **52**, 2364–2367 (1984)
127. M.B. Agranat, S.I. Ashitkov, V.E. Fortov, A.V. Kirillin, A.V. Kostanovskii, S.I. Anisimov, P.S. Kondratenko, Appl. Phys. A Mater. Sci. Process. **69**, 637–640 (1999)
128. B. Lin, H.E. Elsayed-Ali, Surf. Sci. **498**, 275–284 (2002)
129. B.J. Siwick, J.R. Dwyer, R.E. Jordan, R.J.D. Miller, Science **302**, 1382–1385 (2003)
130. K. Sokolowski-Tinten, C. Blome, J. Blums, A. Cavalleri, C. Dietrich, A. Tarasevich, I. Uschmann, E. Förster, M. Kammler, M. Horn-von-Hoegen, D. von der Linde, Nature (London) **422**, 287–289 (2003)
131. J.R. Dwyer, C.T. Hebeisen, R. Ernstorfer, M. Harb, V. Deyirmenjian, R.E. Jordan, R.J.D. Miller, Phil. Trans. R. Soc. A **364**, 741–778 (2006)

132. J.R. Dwyer, R.E. Jordan, C.T. Hebeisen, M. Harb, R. Ernstorfer, T. Dartigalongue, R.J.D. Miller, J. Mod. Optics **54**, 905–922 (2007)
133. C.Y. Ruan, Y. Murooka, R.K. Raman, R.A. Murdick, Nano Lett. **7**, 1290–1296 (2007)
134. W.L. Chan, R.S. Averback, D.G. Cahill, A. Lagoutchev, Phys. Rev. B **78**, 214107 (2008)
135. R. Ernstorfer, M. Harb, C.T. Hebeisen, G. Sciaini, T. Dartigalongue, R.J.D. Miller, Science **323**, 1033–1037 (2009)
136. D.S. Ivanov, L.V. Zhigilei, Phys. Rev. Lett. **98**, 195701 (2007)
137. D.Y. Sun, M. Asta, J.J. Hoyt, Phys. Rev. B **69**, 024108 (2004)
138. F. Celestini, J.-M. Debierre, Phys. Rev. E **65**, 041605 (2002)
139. S.-N. Luo, T.J. Ahrens, T. Çağın, A. Strachan, W.A. Goddard III, D.C. Swift, Phys. Rev. B **68**, 134206 (2003)
140. A.B. Belonoshko, N.V. Skorodumova, A. Rosengren, B. Johansson, Phys. Rev. B **73**, 012201 (2006)
141. A. Vogel, V. Venugopalan, Chem. Rev. **103**, 577–644 (2003)
142. G. Paltauf, P.E. Dyer, Chem. Rev. **103**, 487–518 (2003)
143. I. Itzkan, D. Albagli, M.L. Dark, L.T. Perelman, C. von Rosenberg, M.S. Feld, Proc. Natl. Acad. Sci. U.S.A. **92**, 1960–1964 (1995)
144. A.A. Oraevsky, S.L. Jacques, F.K. Tittel, J. Appl. Phys. **78**, 1281–1290 (1995)
145. R. Cramer, R.F. Haglund, F. Hillenkamp, Int. J. Mass Spectrom. Ion Processes **169/170**, 51–67 (1997)
146. W.H. Duff, L.V. Zhigilei, J. Phys.: Conf. Ser. **59**, 413–417 (2007)
147. S.I. Anisimov, V.V. Zhakhovskii, N.A. Inogamov, K. Nishihara, Yu. V. Petrov, Appl. Surf. Sci. **253**, 6390–6393 (2007)
148. V. Vitek, Philos. Mag. **21**, 1275–1278 (1970)
149. D. Ashkenasi, M. Lorenz, R. Stoian, A. Rosenfeld, Appl. Surf. Sci. **150**, 101–106 (1999)
150. P.T. Mannion, J. Magee, E. Coyne, G.M. O'Connor, T.J. Glynn, Appl. Surf. Sci. **233**, 275–287 (2004)
151. S.E. Kirkwood, A.C. van Popta, Y.Y. Tsui, R. Fedosejevs, Appl. Phys. A **81**, 729–735 (2005)
152. J. Krüger, D. Dufft, R. Koter, A. Hertwig, Appl. Surf. Sci. **253**, 7815–7819 (2007)
153. G. Raciukaitis, M. Brikas, P. Gecys, M. Gedvilas, Proc. SPIE **7005**, 70052L (2008)
154. L.V. Zhigilei, B.J. Garrison, Mat. Res. Soc. Symp. Proc. **538**, 491–496 (1999)
155. C. Schafer, H.M. Urbassek, L.V. Zhigilei, B.J. Garrison, Comp. Mater. Sci. **24**, 421–429 (2002)
156. L.V. Zhigilei, D.S. Ivanov, E. Leveugle, B. Sadigh, E.M. Bringa, in *High-Power Laser AblationV*, ed. by C.R. Phipps. Proceedings of SPIE, vol. 5448, pp. 505–519 (2004)
157. D. Perez, L.J. Lewis, Phys. Rev. B **67**, 184102 (2003)
158. J.-M. Savolainen, M.S. Christensen, P. Balling, Phys. Rev. B **84**, 193410 (2011)
159. A.Y. Vorobyev, C. Guo, Phys. Rev. B **72**, 195422 (2005)
160. A.Y. Vorobyev, C. Guo, Appl. Phys. A **86**, 321–324 (2007)
161. Q.-Z. Zhao, S. Malzer, L.-J. Wang, Opt. Express **15**, 15741–15746 (2007)
162. Y. Dai, M. He, H. Bian, B. Lu, X. Yan, G. Ma, Appl. Phys. A **106**, 567–574 (2012)
163. K.H. Song, X. Xu, Appl. Surf. Sci. **127–129**, 111–116 (1998)
164. J.H. Yoo, S.H. Jeong, X.L. Mao, R. Greif, R.E. Russo, Appl. Phys. Lett. **76**, 783–785 (2000)
165. C. Porneala, D.A. Willis, Appl. Phys. Lett. **89**, 211121 (2006)
166. N.M. Bulgakova, A.V. Bulgakov, Appl. Phys. A **73**, 199–208 (2001)
167. M.M. Martynyuk, Sov. Phys. Tech. Phys. **21**, 430–433 (1976)
168. A. Miotello, R. Kelly, Appl. Phys. A **69**, S67–S73 (1999)
169. R. Kelly, A. Miotello, J. Appl. Phys. **87**, 3177–3179 (2000)
170. B.J. Garrison, T.E. Itina, L.V. Zhigilei, Phys. Rev. E **68**, 041501 (2003)
171. L.V. Zhigilei, A.N. Volkov, E. Leveugle, M. Tabetah, Appl. Phys. A **105**, 529–546 (2011)
172. L.V. Zhigilei, Mat. Res. Soc. Symp. Proc. **677**, AA2.1.1–AA2.1.11 (2001)
173. S. Noël, J. Hermann, T. Itina, Appl. Surf. Sci. **253**, 6310–6315 (2007)

174. T.E. Itina, K. Gouriet, L.V. Zhigilei, S. Noël, J. Hermann, M. Sentis, Appl. Surf. Sci. **253**, 7656–7661 (2007)
175. S. Amoruso, R. Bruzzese, C. Pagano, X. Wang, Appl. Phys. A **89**, 1017–1024 (2007)
176. O. Albert, S. Roger, Y. Glinec, J.C. Loulergue, J. Etchepare, C. Boulmer-Leborgne, J. Perriere, E. Millon, Appl. Phys. A **76**, 319–323 (2003)
177. N. Jegenyes, J. Etchepare, B. Reynier, D. Scuderi, A. Dos-Santos, Z. Tóth, Appl. Phys. A **91**, 385–392 (2008)
178. D. Scuderi, R. Benzerga, O. Albert, B. Reynier, J. Etchepare, Appl. Surf. Sci. **252**, 4360–4363 (2006)
179. I. Apitz, A. Vogel, Appl. Phys. A **81**, 329–338 (2005)
180. A. Vogel, I. Apitz, V. Venugopalan, in *Oscillations, Waves and Interactions*, ed. by T. Kurz, U. Parlitz, U. Kaatze (Universitätsverlag Göttingen, Göttingen, 2007), pp. 217–258
181. E.B. Mpemba, D.G. Osborne, Phys. Educ. **4**, 172–175 (1969)
182. A. Piqué, R.A. McGill, D.B. Chrisey, D. Leonhardt, T.E. Mslna, B.J. Spargo, J.H. Callahan, R.W. Vachet, R. Chung, M.A. Bucaro, Thin Solid Films **355/356**, 536–541 (1999)
183. D.B. Chrisey, A. Piqué, R.A. McGill, J.S. Horwitz, B.R. Ringeisen, D.M. Bubb, P.K. Wu, Chem. Rev. **103**, 553–576 (2003)
184. D.M. Bubb, P.K. Wu, J.S. Horwitz, J.H. Callahan, M. Galicia, A. Vertes, R.A. McGill, E.J. Houser, B.R. Ringeisen, D.B. Chrisey, J. Appl. Phys. **91**, 2055–2058 (2002)
185. K. Rodrigo, P. Czuba, B. Toftmann, J. Schou, R. Pedrys, Appl. Surf. Sci. **252**, 4824–4828 (2006)
186. A.T. Sellinger, E.M. Leveugle, K. Gogick, L.V. Zhigilei, J.M. Fitz-Gerald, J. Vac. Sci. Technol. A **24**, 1618–1622 (2006)
187. R. Pate, A.D. Stiff-Roberts, Chem. Phys. Lett. **477**, 406–410 (2009)
188. A.P. Caricato, M. Anni, M.G. Manera, M. Martino, R. Rella, F. Romano, T. Tunno, D. Valerini, Appl. Surf. Sci. **255**, 9659–9664 (2009)
189. A.P. Caricato, G. Leggieri, M. Martino, A. Vantaggiato, D. Valerini, A. Cretì, M. Lomascolo, M.G. Manera, R. Rella, M. Anni, Appl. Phys. A **101**, 759–764 (2010)
190. D.M. Bubb, J. Corgan, S.Y. Yi, M. Khan, L. Hughes, U. Gurudas, M. Papantonakis, R.A. McGill, Appl. Phys. A **100**, 523–531 (2010)
191. S. Guha, D. Adil, N.B. Ukah, R.K. Gupta, K. Ghosh, Appl. Phys. A **105**, 547–554 (2011)
192. Y. Guo, A. Morozov, D. Schneider, J.W. Chung, C. Zhang, M. Waldmann, N. Yao, G. Fytas, C.B. Arnold, R.D. Priestley, Nature Mater. **11**, 337–343 (2012)
193. K.B. Shepard, Y. Guo, C.B. Arnold, R.D. Priestley, Appl. Phys. A **110**, 771–777 (2013)
194. L.V. Zhigilei, C. Wei, D. Srivastava, Phys. Rev. B **71**, 165417 (2005)
195. A.N. Volkov, L.V. Zhigilei, J. Phys. Chem. C **114**, 5513–5531 (2010)
196. A.N. Volkov, L.V. Zhigilei, ACS Nano **4**, 6187–6195 (2010)
197. A.T. Sellinger, A.H. Martin, J.M. Fitz-Gerald, Thin Solid Films **516**, 6033–6040 (2008)
198. Á.P. del Pino, E. György, L. Cabana, B. Ballesteros, G. Tobias, Carbon **50**, 4450–4458 (2012)
199. Animated sequences of snapshots from MD simulations of laser melting, spallation, and ablation can be found at http://www.faculty.virginia.edu/CompMat/Resources.html
200. L.A. Falkovsky, E.G. Mishchenko, J. Exp. Theor. Phys. **88**, 84–88 (1999)
201. Y. Gan, J.K. Chen, Appl. Phys. Lett. **94**, 201116 (2009)
202. Y. Gan, J.K. Chen, J. Appl. Phys. **108**, 103102 (2010)
203. G.E. Norman, S.V. Starikov, V.V. Stegailov, J. Exp. Theor. Phys. **114**, 792–800 (2012)
204. G. Norman, S. Starikov, V. Stegailov, V. Fortov, I. Skobelev, T. Pikuz, A. Faenov, S. Tamotsu, Y. Kato, M. Ishino, M. Tanaka, N. Hasegawa, M. Nishikino, T. Ohba, T. Kaihori, Y. Ochi, T. Imazono, Y. Fukuda, M. Kando, T. Kawachi, J. Appl. Phys. **112**, 013104 (2012)
205. L. Shokeen, P.K. Schelling, Appl. Phys. Lett. **97**, 151907 (2010)
206. L. Shokeen, P.K. Schelling, J. Appl. Phys. **109**, 073503 (2011)
207. L. Shokeen, P.K. Schelling, Comput. Mater. Sci. **67**, 316–328 (2013)
208. S. Khakshouri, D. Alfè, D.M. Duffy, Phys. Rev. B **78**, 224304 (2008)
209. Z. Lin, L.V. Zhigilei, Proc. SPIE **6261**, 62610U (2006)

210. Z. Lin, L.V. Zhigilei, Appl. Surf. Sci. **253**, 6295–6300 (2007)
211. C. Suárez, W.E. Bron, T. Juhasz, Phys. Rev. Lett. **75**, 4536–4539 (1995)
212. Z. Chen, V. Sametoglu, Y.Y. Tsui, T. Ao, A. Ng, Phys. Rev. Lett. **108**, 165001 (2012)
213. B. Rethfeld, A. Kaiser, M. Vicanek, G. Simon, Phys. Rev. B **65**, 214303 (2002)
214. W. Wendelen, B.Y. Mueller, D. Autrique, B. Rethfeld, A. Bogaerts, J. Appl. Phys. **111**, 113110 (2012)
215. N. Medvedev, U. Zastrau, E. Förster, D.O. Gericke, B. Rethfeld, Phys. Rev. Lett. **107**, 165003 (2011)
216. G.A. Bird, *Molecular Gas Dynamics and the Direct Simulation of Gas Flows* (Clarendon Press, Oxford, 1994)
217. H.M. Urbassek, D. Sibold, Phys. Rev. Lett. **70**, 1886–1889 (1993)
218. O. Ellegaard, J. Schou, H.M. Urbassek, Appl. Phys. A **69**, S577–S582 (1999)
219. T.E. Itina, J. Appl. Phys. **89**, 740–746 (2001)
220. T.E. Itina, W. Marine, M. Autric, J. Appl. Phys. **82**, 3536–3542 (1997)
221. A.A. Morozov, Phys. Fluids **19**, 087101 (2007)
222. G.A. Lukyanov, Y. Khang, D.V. Leshchev, S.V. Kozyrev, A.N. Volkov, N.Y. Bykov, O.I. Vakulova, Fuller. Nanotub. Car. N **14**, 507–512 (2006)
223. T.E. Itina, M. Sentis, W. Marine, Appl. Surf. Sci. **252**, 4433–4438 (2006)
224. A.N. Volkov, G.M. O'Connor, T.J. Glynn, G.A. Lukyanov, Appl. Phys. A **92**, 927–932 (2008)
225. A.N. Volkov, L.V. Zhigilei, Appl. Phys. A **110**, 537–546 (2013)
226. M.I. Zeifman, B.J. Garrison, L.V. Zhigilei, J. Appl. Phys. **92**, 2181–2193 (2002)
227. M.I. Zeifman, B.J. Garrison, L.V. Zhigilei, Appl. Surf. Sci. **197/198**, 27–34 (2002)
228. T. E. Itina and L. V. Zhigilei, J. Phys.: Conf. Ser. **59**, 44–49 (2007)